

Something something something physics

Steven Green
of Emmanuel College

A dissertation submitted to the University of Cambridge
for the degree of Doctor of Philosophy

Abstract

LHCb is a b-physics detector experiment which will take data at the 14 TeV LHC accelerator at CERN from 2007 onward...

Declaration

This dissertation is the result of my own work, except where explicit reference is made to the work of others, and has not been submitted for another qualification to this or any other university. This dissertation does not exceed the word limit for the respective Degree Committee.

Andy Buckley

Acknowledgements

Of the many people who deserve thanks, some are particularly prominent, such as my supervisor...

Preface

This thesis describes my research on various aspects of the LHCb particle physics program, centred around the LHCb detector and LHC accelerator at CERN in Geneva.

For this example, I'll just mention Chapter ?? and Chapter ??.

Contents

1. Calorimeter Optimisation Studies	1
1.1. Calorimeter Optimisation Studies	1
1.2. Metric	2
1.3. Simulation and Reconstruction	2
1.4. Calibration	2
1.5. Nominal Detector Performance	2
1.6. Electromagnetic Calorimeter Optimisation	3
1.6.1. ECal Transverse Granularity	4
1.6.2. ECal Longitudinal Granularity	6
1.6.3. ECal Active Material	9
1.7. Hadronic Calorimeter Optimisation	10
1.7.1. HCal Transverse Granularity	11
1.7.2. HCal Longitudinal Granularity	13
1.7.3. HCal Depth	15
2. The Sensitivity of CLIC to Anomalous Gauge Couplings through Vector Boson Scattering	19
2.1. Background	19
2.2. Generation	20
2.2.1. Cross Section Sensitivity	20
2.2.2. Anomalous Gauge Coupling Event Weights	22
2.2.3. Validation of Samples	22
2.3. Simulation and Reconstruction	24
2.3.1. Experimental Conditions at CLIC	26
2.4. Analysis	28
2.4.1. Jet Pairing	28
2.4.2. Isolated Lepton Finding	30
2.4.3. Flavour Tagging	31

2.4.4. Analysis Processor	31
2.5. Fitting Technique	33
2.5.1. Choice of Fitting Distribution	33
2.5.2. Application Of Anomalous Gauge Coupling Event Weights	34
2.5.3. Analysis of Fitting Distribution	37
2.6. Optimisation of Jet Reconstruction	38
2.6.1. 1.4 TeV Optimal Jet Reconstruction	38
2.6.2. 3 TeV Optimal Jet Reconstruction	38
2.7. Event Selection	42
2.7.1. Pre Selection - 1.4 TeV	42
2.7.2. MVA - 1.4 TeV	44
2.7.3. Pre Selection - 3 TeV	50
2.7.4. MVA - 3 TeV	50
2.8. Results	50
2.8.1. 1.4 TeV	50
A. Pointless extras	55
A.1. Anomalous Gauge Coupling Quartic Vertices Of Relevance in Vector Boson Scattering	55
A.2. χ^2 Contour Plots for Jet Algorithm Optimisation	58
Bibliography	67
List of figures	69
List of tables	73

*“Writing in English is the most ingenious torture
ever devised for sins committed in previous lives.”*

— James Joyce

Chapter 1.

Calorimeter Optimisation Studies

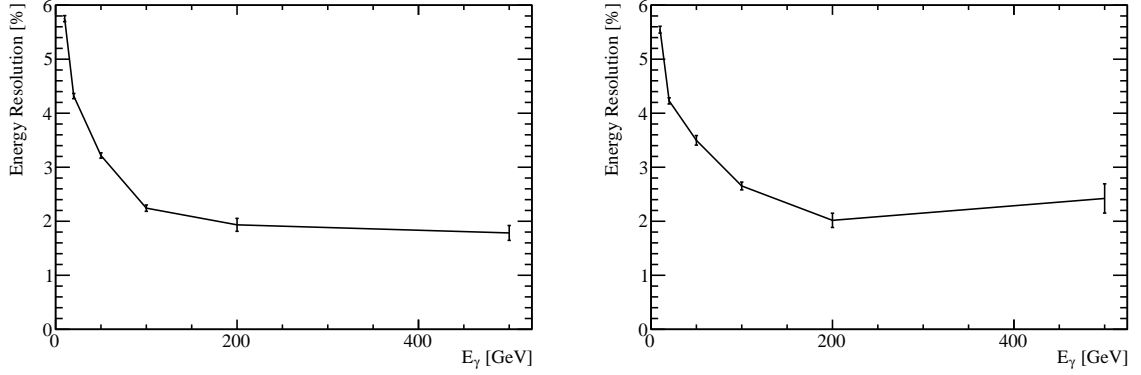
“There, sir! that is the perfection of vessels!”

— Jules Verne, 1828–1905

1.1. Calorimeter Optimisation Studies

If the future linear collider is to reach its maximum potential in terms of energy resolution then, optimisation of the detector will be essential. The energy resolution in the particle flow paradigm is dependant upon several detector components. The momentum of charged particles arises from the shape of the tracks deposited within the detector while the energy of uncharged particles arise from calorimetric measurements. Application of sophisticated pattern recognition algorithms allows the particle type to be inferred for the charged particles. In turn this allows for the conversion of the track momentum into an energy measure for the charged particles. The particle identification algorithms use the topological information acquired from the calorimetric energy deposited to infer particle type for a subset of charged particles.

The calorimetric energy deposits are therefore used in a twofold manner: (i) as energy measurements for neutral particles and (ii) as input for particle identification algorithms. There is potential for significant gains to be made in physics performance by optimising the calorimeters due to their dominant role in energy measurements. In this chapter the optimisation of the calorimeters is considered. Parameters such



(a) Silicon active material, $5 \times 5 \text{ mm}^2$ ECal transverse granularity.
(b) Scintillator active material, $5 \times 5 \text{ mm}^2$ ECal transverse granularity.

Figure 1.1.: Energy resolution as a function of photon energy for the nominal ILD detector for both the silicon and scintillator options.

as the longitudinal granularity, transverse granularity and material choices for the calorimeters are considered.

This chapter concludes with an optimisation of several global parameters for the detector. These parameters are not calorimeter specific, but the optimisation procedure developed for the calorimeters is appropriate to use. These parameters relate to the global detector size and the magnetic field applied throughout solenoid in the detector.

1.2. Metric

1.3. Simulation and Reconstruction

1.4. Calibration

1.5. Nominal Detector Performance

The energy resolution for single photon events as a function of photon energy, for the nominal ILD detector, is shown in figure 1.1. The nominal jet energy resolution can be found in section BLAH.

1.6. Electromagnetic Calorimeter Optimisation

The ECal primarily measures the energy deposits of electromagnetic showers. The default ILD detector model ECal, summarised in table 1.1, contains 24 radiation lengths (X_0 , which acts to confine all but the highest energy electromagnetic showers within it. The longitudinal structure of this default model is 29 readout layers, consisting of pairs of active and absorber material, and one presampling layer, which exists to encourage shower development. Increasing the thickness of the absorber material part way into the detector reduces the number of readout channels and cost of the overall calorimeter while retaining a high sampling rate at the start of particle showers, which is crucial for the pattern recognition aspect of particle flow calorimetry.

Parameter	Default Value
Transverse Granularity	$5 \times 5\text{mm}^2$ square cells
Longitudinal Granularity	29 Readout Layers, 1 Presampling Layers
Active Material Choice	Silicon or Scintillator
Active Material Thickness	0.5 mm (Silicon) or 2 mm (Scintillator)
Absorber Material Choice	Tungsten
Absorber Material Thickness	20 Layers of 2.1 mm followed by 9 Layers of 4.2 mm

Table 1.1.: Nominal ILD detector model ECal configuration.

The parameters being optimised in this study are:

- Transverse granularity or cell size. This is a vital aspect of the detector in the particle flow paradigm as smaller cell sizes give greater potential for being able to separate energy deposits from charged and neutral particles. This transverse granularity should have little to no effect on the intrinsic energy resolution of the detector.
- Longitudinal granularity or cell depth. This parameter dictates the intrinsic energy resolution of the detector as smaller cell depths mean more sampling is done of the particle shower and so, due to the Poissonian statistics governing the measurement of particle showers, the better the resolution.
- Active material choice. This is a choice between silicon or scintillator. As well as providing different intrinsic energy resolutions the readout mechanics of these

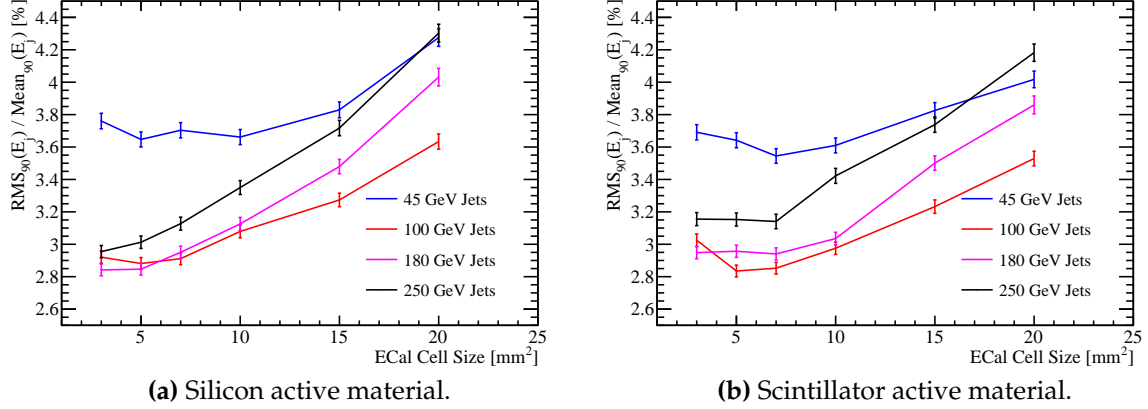


Figure 1.2.: Jet energy resolution as a function of ECal cell size for the silicon and scintillator ECal options.

two options are significantly different. There is no clear prior knowledge as to which should provide better performance.

1.6.1. ECal Transverse Granularity

For this study a number of different detector models were considered where the transverse granularity in the ECal had been varied about the nominal value of $5 \times 5\text{mm}^2$ square cells. The granularities considered were $3 \times 3\text{mm}^2$, $5 \times 5\text{mm}^2$, $7 \times 7\text{mm}^2$, $10 \times 10\text{mm}^2$, $15 \times 15\text{mm}^2$ and $20 \times 20\text{mm}^2$ square cells for both the silicon and scintillator active material options. The jet energy resolution as a function of transverse granularity in the ECal is shown in figure 1.2.

The jet energy resolution was found to improve with decreasing cell size. This is expected as smaller cell size lead to better separation of energy deposits from neutral and charged particle showers.

By examining the breakdown of the jet energy resolution into intrinsic resolution and confusion terms, as explained in chapter BLAH, it is possible to conclude that the dominant factor affecting the jet energy resolution when the transverse granularity of the ECal is varied is the confusion arising from photon energy deposits. Examples of jet energy resolution breakdowns are shown for 45 and 250 GeV jets for both the silicon and scintillator ECal options in figure 1.3. As expected in the intrinsic energy resolution does not change significantly with the transverse granularity.

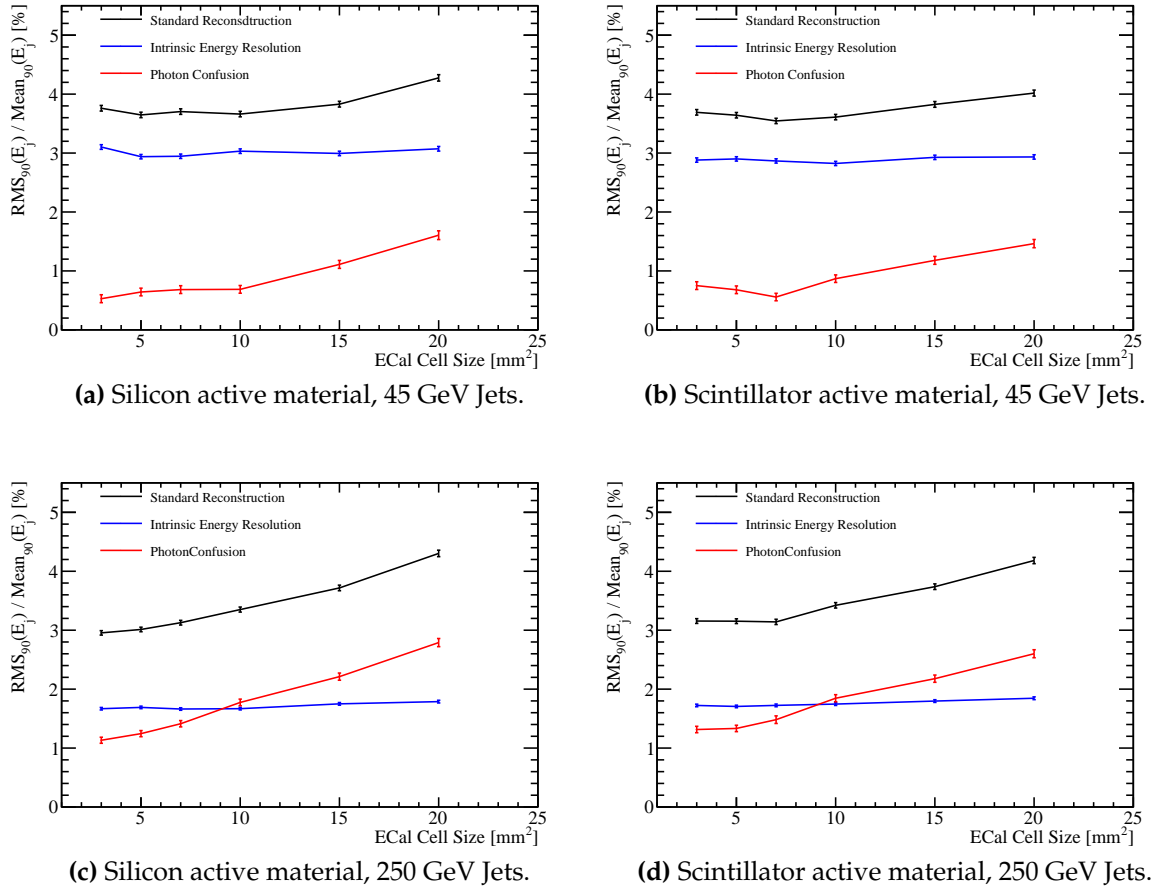


Figure 1.3.: Jet energy resolution breakdown as a function of ECal transverse granularity for 45 and 250 GeV jets. Results are given for both the silicon and scintillator ECal options.

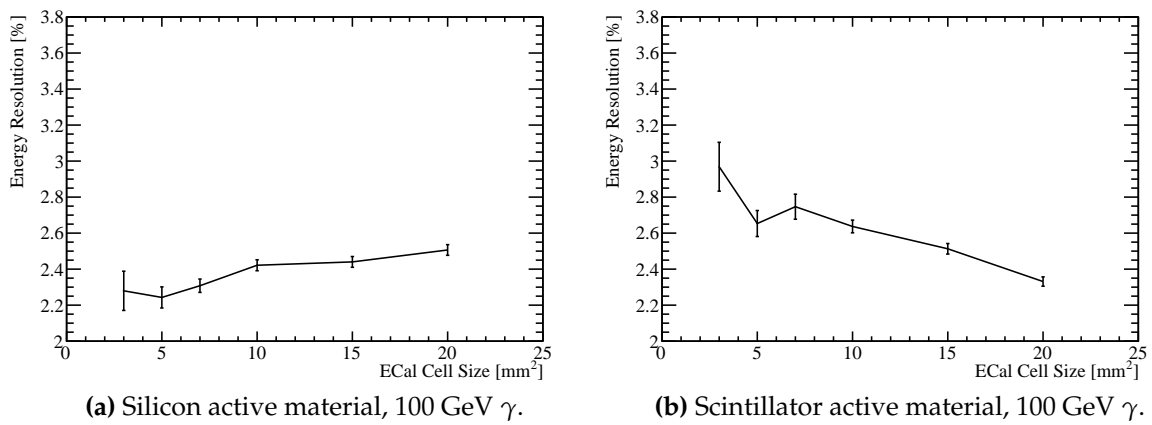


Figure 1.4.: Energy resolution as a function of ECal transverse granularity for 100 GeV photons. Results are given for both the silicon and scintillator ECal options.

A more targeted test of the intrinsic energy resolution of the ECal is presented in figure 1.4, which examines the energy resolution of single photon samples at 100 GeV. For the silicon option the intrinsic energy resolution was found to not vary significantly across the transverse granularities under consideration, however, there is a degradation in energy resolution with increasing cell size for the scintillator option. This originates from an inactive region of material in the simulation that represents the multi pixel photon counter (MPPC). The MPPC occupies a fixed area of the cell irrespective of cell size and so fractionally the "dead" region of the cell increases as cell size is reduced (cite this somehow). These trends will be present in the jet energy resolution studies, however, as only a small fraction, $\approx 10\%$, of the jet energy arises from the ECal these trends will be washed out when looking purely at jets.

In conclusion smaller transverse granularities in the ECal significantly improve the jet energy resolution for both the silicon and scintillator options. The intrinsic energy resolution of the ECal is largely invariant to changes in the transverse granularity for the silicon option, while larger transverse granularities are beneficial to the scintillator option as they reduce the impact of "dead" regions of the detector.

1.6.2. ECal Longitudinal Granularity

The performance of a number of detector configurations was examined where the longitudinal granularity of the ECal absorber material had been varied about the nominal value. This study was performed for both the silicon and scintillator active material options. In all cases considered tungsten was used as the absorber material in the ECal and the active layer thicknesses were not changed, that is 0.5 mm for the silicon option and 2 mm for the scintillator option. The layout of the ECal for detector models considered are summarised in table 1.2. For each detector model considered in this study the total number of radiation lengths in the ECal is kept approximately constant. This is done by varying the thickness of the absorber material when modifying the number of layers in the ECal.

The jet energy resolution was found to improve with increasing longitudinal granularity. This is expected as a more layers in the calorimeter, for the same total thickness, implies greater sampling of the particle shower and so, as the energy resolution obeys Poissonian statistics, an improvement in the intrinsic energy resolution is observed.

Total Number of Layers	N_{Layers} Region 1	Absorber Thickness	N_{Layers} Region 2	Absorber Thickness	Total Thickness $[X_0]$
N_{Layers} ECal	Region 1 [mm]			Region 2 [mm]	
30	20	2.10	9	4.20	22.77
26	17	2.40	8	4.80	22.60
20	13	3.15	6	6.30	22.47
16	10	4.00	5	8.00	22.31

Table 1.2.: Transverse granularity layout of various ECal models considered in this study. Radiation length of tungsten absorber is 3.504mm [12]. Note that the presampler layer contributes one layer to the cumulative number of layers value for all detector models considered.

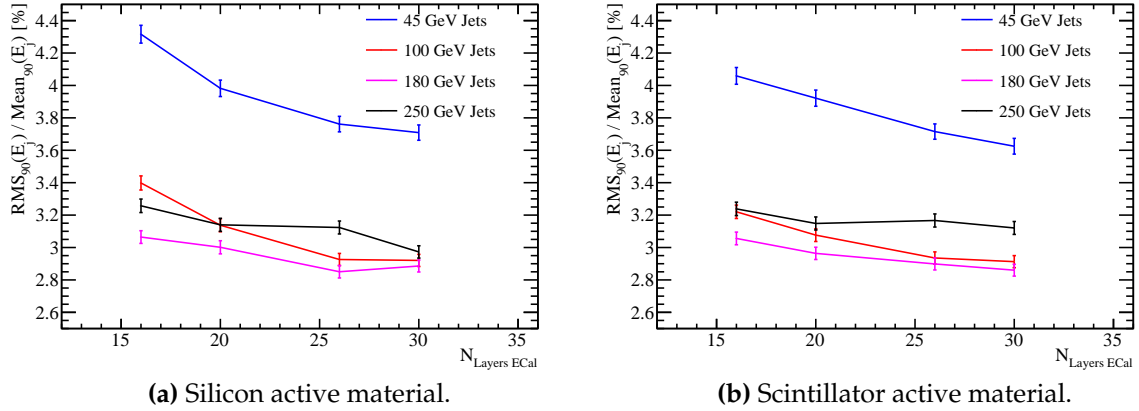


Figure 1.5.: Jet energy resolution as a function of longitudinal granularity in the ECal for the silicon and scintillator ECal options.

A particularly strong dependency on ECal longitudinal granularity is noted at low energies, but this reduces significantly as energies rise.

The strong dependency of the jet energy resolution on the ECal longitudinal granularity can be expanded upon by looking at the decomposition of the jet energy resolution, which is shown in figure 1.6 for the 45 and 250 GeV energy jets. At low energies the trend is twofold: an improvement to the intrinsic energy resolution with more sampling of particle showers and a reduction in the impact of confusion. For high energy jets, where confusion dominates, there is little to no change in the intrinsic energy resolution and confusion as a function of ECal transverse granularity.

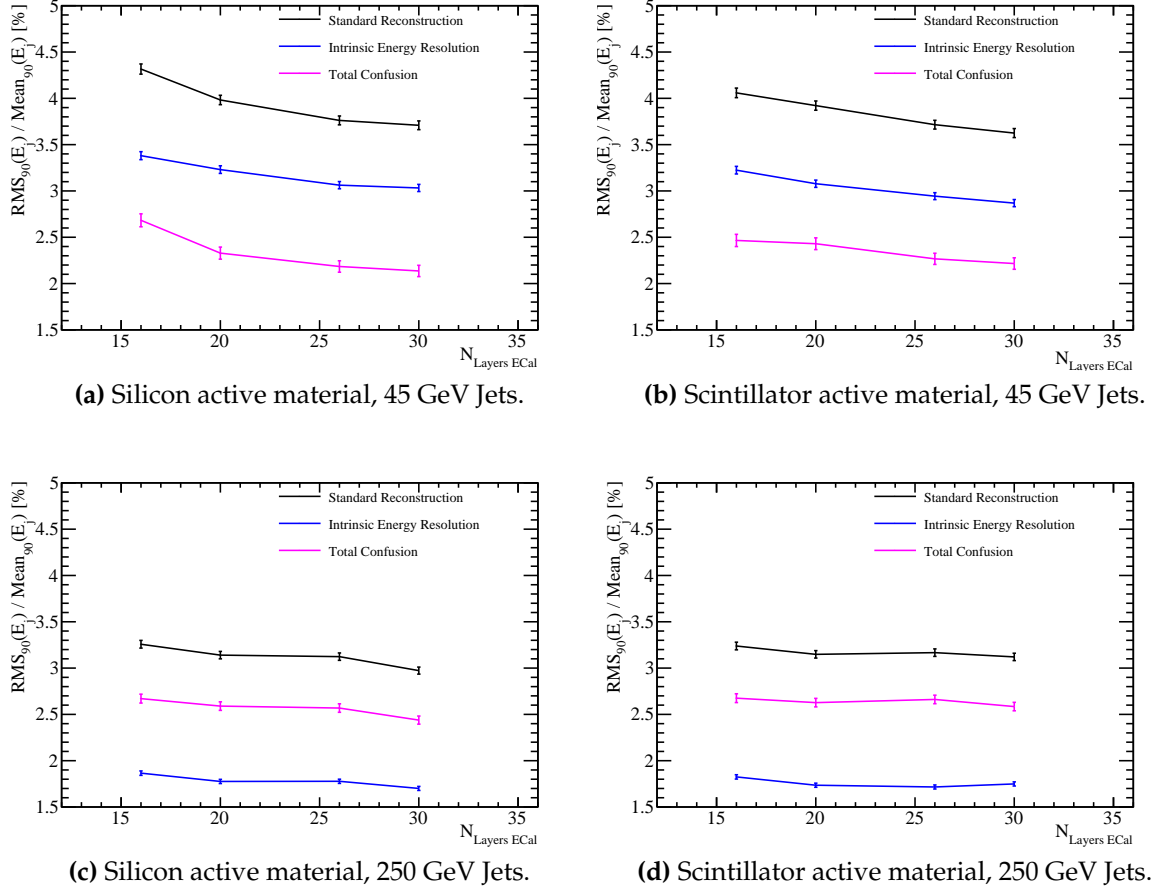


Figure 1.6.: Jet energy resolution breakdown as a function of ECal longitudinal granularity for 45 and 250 GeV jets. Results are given for both the silicon and scintillator ECal options.

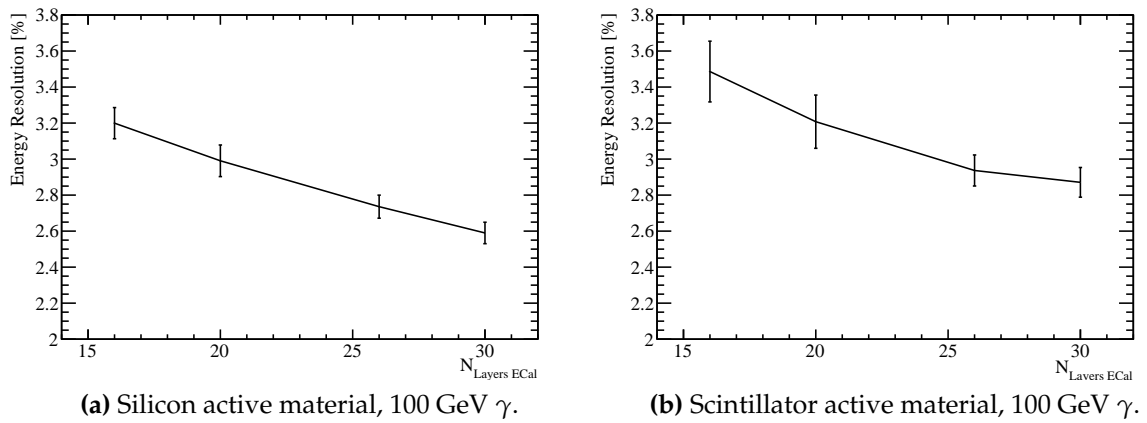


Figure 1.7.: Energy resolution as a function of function of ECal longitudinal granularity for 100 GeV photons. Results are given for both the silicon and scintillator ECal options.

Further understanding is gained by considering the energy resolution of single photon samples at 100 GeV as a function of the longitudinal granularity in the ECal, which is shown in figure 1.7. At these large photon energies it is clear that the intrinsic energy resolution of the ECal is improved by having finer longitudinal segmentation in the ECal. This trend will be present in the jet energy resolution study, but as only $\approx 10\%$ of the jet energy is measured in the ECal in comparison to $\approx 100\%$ of the photons energy, it will be obscured by the energy resolution of the rest of the detector, which is invariant to the ECal longitudinal segmentation.

The intrinsic energy resolution of the ECal is improved by having a finer transverse granularity. This is evident when looking at the energy resolution of photons whose energy deposits are localised within the ECal. This trend is again clear when considering the energy resolution of low energy jets, however, at higher energies the longitudinal granularity in the ECal is not a significant factor in determining detector performance.

1.6.3. ECal Active Material

In sections 1.6.1 and 1.6.2 the performance of the ECal was reported for both the silicon and scintillator options and to a large extent the performance of the two options was the same. There were a few differences, which attention should be brought to:

- The intrinsic energy resolution of a silicon ECal is worse than that of a scintillator ECal for low energies, while the trend is reversed at high energies. The cross over point in performance occurs between 20 and 50 GeV. This trend is shown in figure 1.1.
- The "dead" region due to the presence of the MPPC in the scintillator option degrades performance of the detector for small transverse granularities. No such effect is seen for the silicon option. This effect is shown in figure 1.4.

The lack of this "dead" region of the detector and the beneficial intrinsic energy resolution at large energies indicates a preference for a silicon detector, however, there is no clear preference based on these studies.

1.7. Hadronic Calorimeter Optimisation

The HCal is designed to measure the energy deposits from hadrons. The default ILD detector model HCal, summarised in table 1.3, contains ≈ 6 nuclear interaction lengths (λ_I). The ECal contributes approximately one λ_I giving a total of $\approx 7\lambda_I$, which is sufficient to confine the bulk of jets up to 1 TeV events, which is the maximum running energy for the ILC. The longitudinal structure of this model consists of 48 readout layers each containing a 3 mm active layer of scintillator and a 20 mm absorber layer of iron. There are several readout technology options under consideration for the HCal, which are analogue, digital and semi-digital, however, for this study only the analogue HCal is considered.

Parameter	Default Value
Transverse Granularity	$30 \times 30\text{mm}^2$ square cells
Longitudinal Granularity	48 Readout Layers
Active Material Choice	Scintillator Tiles
Active Material Thickness	3 mm
Absorber Material Choice	Steel
Absorber Material Thickness	20 mm

Table 1.3.: Nominal ILD detector model HCal configuration.

The parameters being optimised in this study are:

- Transverse granularity or cell size. This is key to successful application of pattern recognition in the particle flow paradigm, but should not change intrinsic energy resolution.
- Longitudinal granularity or cell depth. This governs the intrinsic energy resolution of a calorimeter.
- Depth of calorimeter. This is important in determining the impact of leakage of energy out of the detector.
- Sampling fraction. This is the ratio of the active medium thickness to the absorber medium thickness. As sampling calorimetry is based on sampling of particle showers it is expected that this is an important parameter. However, above a given sampling fraction there should be little difference between performance if

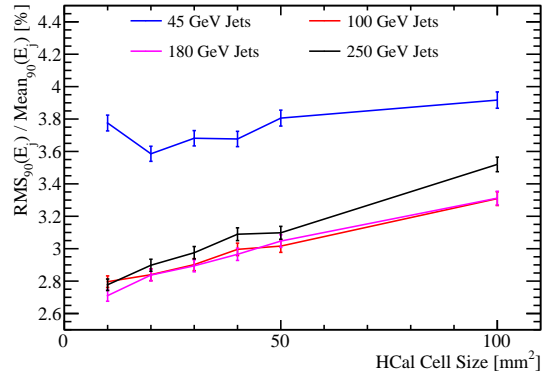


Figure 1.8.: Jet energy resolution as a function of HCal cell size.

showers are sampled at a high enough rate to get a good estimate of the incoming particles energy.

- Absorber material choice. This is a choice between steel or tungsten. While this does not change the active medium choice it does dictate the growth and propagation of showers and so plays a crucial role in calorimetry. While tungsten is more expensive than steel for the raw material the larger number of interaction lengths per length scale for tungsten mean that it is possible to create a smaller detector with the same number of interaction lengths within it. This reduces the size of the solenoid needed to generate the magnetic field and so lowers the price of the detector. As both of these materials are viable as absorber medium choices it is crucial to determine if either is more advantageous from a physics perspective.

1.7.1. HCal Transverse Granularity

For this study a number of different detector models were considered where the transverse granularity in the HCal had been varied about the nominal value of $30 \times 30\text{mm}^2$ square cells. The granularities considered were $10 \times 10\text{mm}^2$, $20 \times 20\text{mm}^2$, $30 \times 30\text{mm}^2$, $40 \times 40\text{mm}^2$, $50 \times 50\text{mm}^2$ and $100 \times 100\text{mm}^2$ square cells. The jet energy resolution as a function of transverse granularity in the HCal is shown in figure 1.8.

As with the case for the ECal, the jet energy resolution was found to improve with decreasing cell size as smaller cell size lead to better separation of energy deposits from neutral and charged particle showers.

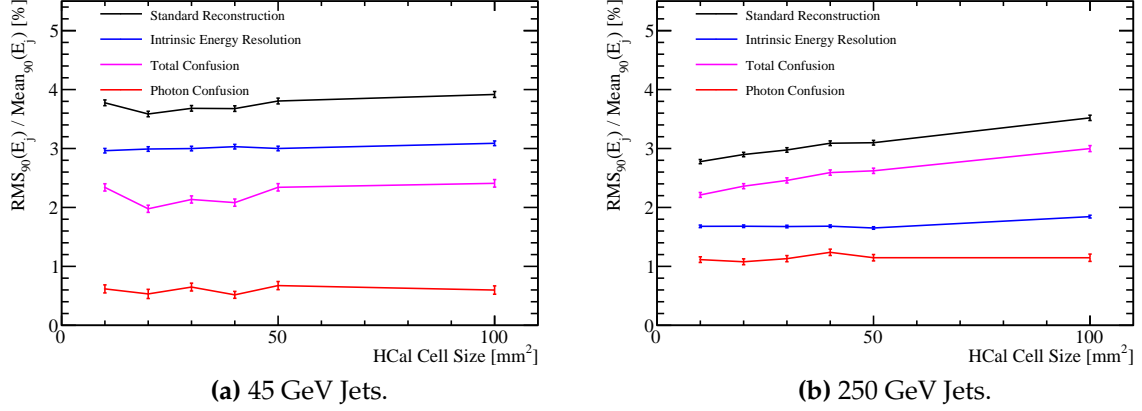


Figure 1.9.: Jet energy resolution breakdown as a function of HCal transverse granularity for 45 and 250 GeV jets.

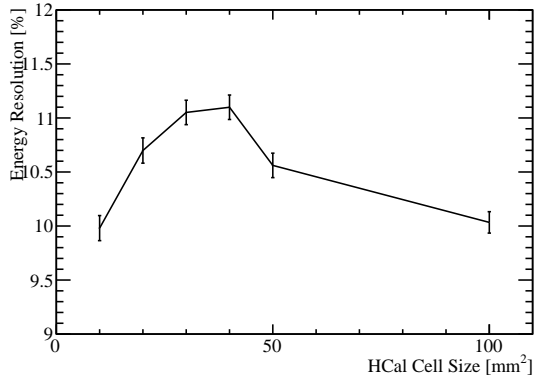


Figure 1.10.: Energy resolution as a function of HCal transverse granularity for 50 GeV K_L^0 .

The jet energy resolution breakdowns, shown in figure 1.9, show that the confusion term varies when changing the HCal transverse granularity, but the intrinsic energy resolution does not. Furthermore, the photon confusion is invariant to changes in HCal transverse granularity, indicating that the observed overall performance changes are due to the effects of confusion arising from energy deposits from charged and neutral hadrons. Once again for 45 GeV jets the detector performance is dominated by intrinsic energy resolution and so HCal transverse granularity has little effect, while for 250 GeV jets the performance is dominated by confusion and HCal transverse granularity becomes more significant.

The energy resolution of single long lived neutral kaons, K_L^0 , at 50 GeV is considered as a function of transverse granularity in the HCal. This is shown in figure 1.10 and, as expected, the energy resolution of the detector is largely invariant to changes in

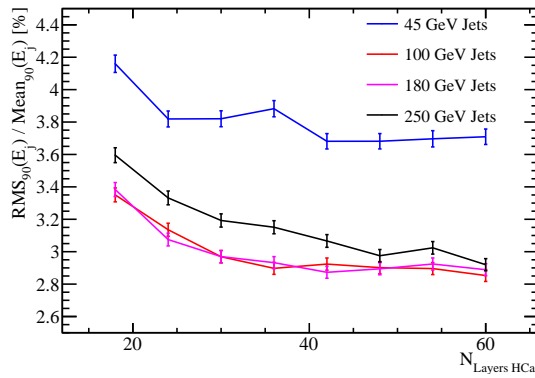


Figure 1.11.: Jet energy resolution as a function of longitudinal granularity in the HCal.

the transverse granularity in the HCal. As these K_L^0 samples may deposit energy in the ECal, this figure represents the intrinsic energy resolution of the ILD detector as a whole and not purely that of the HCal. However, it is expected that the bulk of the energy deposited by these samples occurs within the HCal and so such plots are a useful representation of the HCal performance.

The transverse granularity of the HCal acts to determine the impact of confusion from charged and neutral hadron energy deposits. It does not vary the intrinsic energy resolution of the detector, nor does it impact the reconstruction of photons. As confusion is dominant at high jet energies the HCal transverse granularity gains an increasing role in determining detector performance as the energy in an event increases.

1.7.2. HCal Longitudinal Granularity

A number of different detector models were examined where the longitudinal granularity of the HCal had been varied about the nominal value. In all cases the absorber material was steel while the active material was scintillator. Each HCal configuration had the same total number of nuclear interaction lengths, $5.72 \lambda_I$ in the absorber material and $0.19 \lambda_I$ in the active material, however, the thickness of the layers was varied depending on the total number of layers being considered. The ratio of the active material layers to the absorber material layers, the sampling fraction, was also kept constant in this study. A summary of the detector models considered in this study can be found in table 1.4.

Number $N_{\text{Layers HCal}}$	Absorber Thickness	Active Thickness
	[mm]	[mm]
60	16.00	2.40
54	17.78	2.67
48	20.00	3.00
42	22.86	3.43
36	26.67	4.00
30	32.00	4.80
24	40.00	6.00
18	53.33	8.00

Table 1.4.: Transverse granularity layout of various HCal models considered.

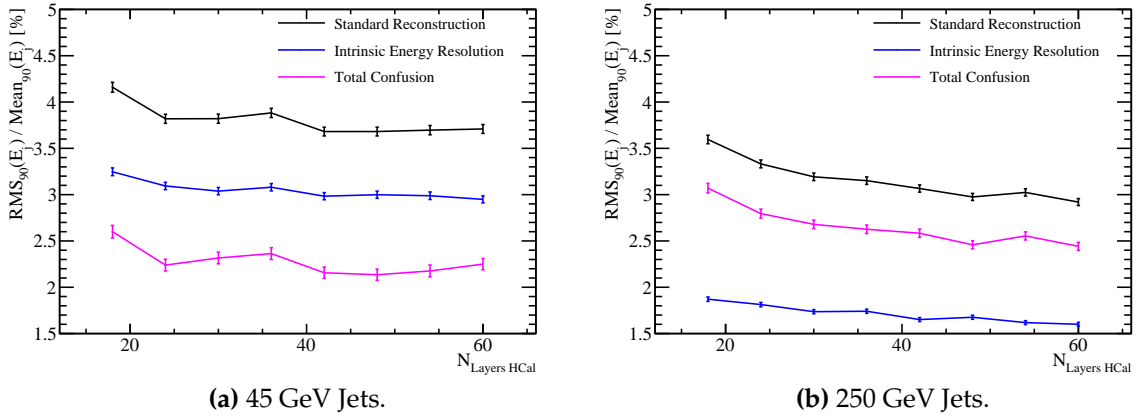


Figure 1.12.: Jet energy resolution breakdown as a function of HCal longitudinal granularity for 45 and 250 GeV jets.

The jet energy resolution for the various detector models considered is shown in figure 1.13. It was found that increasing the number of layers in the HCal, for the same total thickness, improved the jet energy resolution for all jet energies considered. Based on the increase in the frequency of sampling of particle showers in the HCal, it is expected that the intrinsic energy resolution of the detector should improve. However, the improvement observed in jet energy resolution for high energy jets indicates that longitudinal granularity is also affecting the confusion terms.

These trends are further explored by considering the breakdown of jet energy resolution, which are shown in figure 1.12. As expected from the standard performance reconstruction trends as a function of jet energy, there is an improvement in both the

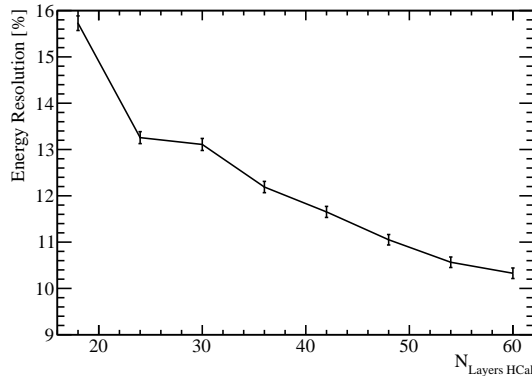


Figure 1.13.: Energy resolution as a function of HCal longitudinal granularity for 50 GeV K_L^0 .

intrinsic energy resolution and a reduction in the impact of confusion when the number of layers in the HCal is increased. The dominant trend driving the overall detector performance is that associated with the confusion of separating energy deposits from charged and neutral particles. This emphasises the importance of pattern recognition to detector performance in the particle flow paradigm.

The change in the intrinsic energy resolution of the HCal when varying the longitudinal granularity is best summarised by looking at the energy resolution of neutral hadrons as in the particle flow paradigm the energy of neutral hadrons is primarily measured in the HCal. A plot of energy resolution against the number of layers in the HCal for 50 GeV K_L^0 can be found in figure 1.13. This data shows that a reduction in sampling frequency of a particle shower that accompanies a reduction in the number of readout layers results in a broadening of energy distributions and a degradation in the resolution. It should again be emphasised that these results are for the full ILD detector model and so include the effect of the $\approx 1\lambda_I$ in the ECal.

The increasing the HCal longitudinal granularity has a twofold effect on the detector performance: an increase in sampling rate of particle showers and an improvement to the intrinsic energy resolution and a reduction in the confusion arising from associating energy deposits from hadrons.

1.7.3. HCal Depth

In this section the total depth of the HCal is varied about the nominal value of $5.72 \lambda_I$ keeping the total number of readout layers fixed at 48, the active material as scintillator,

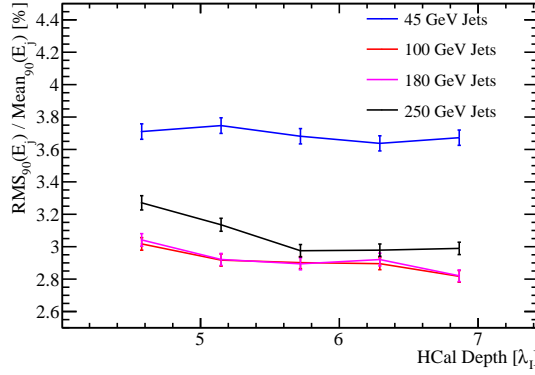


Figure 1.14.: Jet energy resolution is shown for several fixed energy jets as a function of the number of nuclear interaction lengths in the HCal.

the absorber material as iron and ratio of the thicknesses of the active to absorber layers fixed. The details of the detector models considered in this study can be found in table 1.5

HCal Depth [λ_I]	Absorber Thickness [mm]	Active Thickness [mm]
4.58	16	2.4
5.15	18	2.7
5.72	20	3.0
6.29	22	3.3
6.86	24	3.6

Table 1.5.: Depth and layout of various HCal models considered.

The jet energy resolution as a function of the total depth in the HCal is shown in figure 1.14. There is little variation in the detector performance as a function of the total depth of the HCal for all but the highest energy jets. At high jet energies there is a slight degradation in detector performance as the total thickness of the HCal is reduced.

Examining the breakdown of these trends at high energies, shown in figure 1.15, it becomes clear that the degradation in performance is due to confusion in associating energy deposits from hadrons. This is somewhat unexpected as it would be neutral to assume any improvements with a deeper HCal would be due to a reduction in the impact of leakage out of the back of the detector. This may be partially masked by

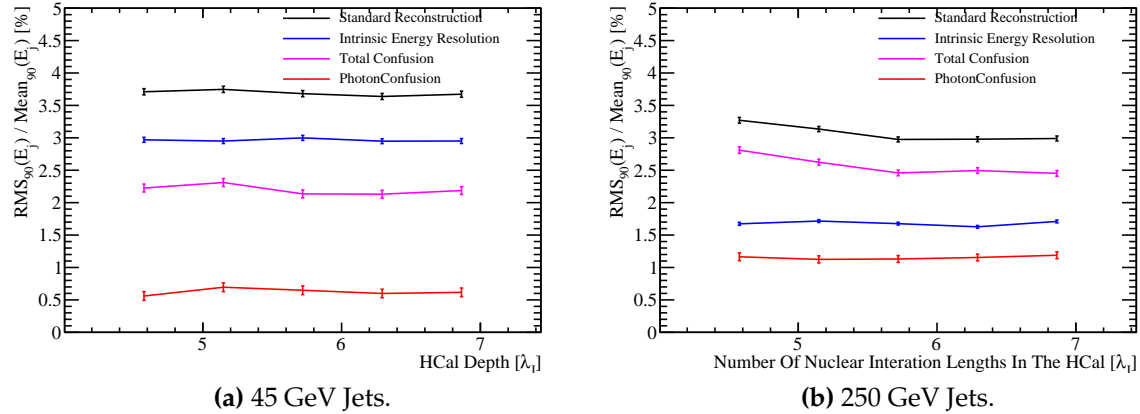


Figure 1.15.: Jet energy resolution breakdown as a function of nuclear interaction lengths in the HCal for 45 and 250 GeV jets.

the definition of RMS90 (PLOT?), however, it is clear that leakage is not a significant problem across the depth of HCals considered here for a typical event at these energies.

INTRINSIC ENERGY RESOLUTION FOR HIGH ENERGIES? HERE

Chapter 2.

The Sensitivity of CLIC to Anomalous Gauge Couplings through Vector Boson Scattering

“Kids, you tried your best, and you failed miserably. The lesson is, never try.”

— Homer Simpson

2.1. Background

A potential source of beyond the standard model physics that could be studied at the CLIC experiment is that of the anomalous gauge couplings α_4 and α_5 . The theoretical basis for these couplings is described in section THEORY REF. CLIC would show sensitivity to these couplings through vector boson scattering processes that are summarised in figures ??, ??, ?? and ?. An analysis of the sensitivity of CLIC to this processes is presented in the following chapter.

2.2. Generation

The event generation software used by the CLIC experiment is Whizard [7, 11]. Whizard version 1.97 was used for generating the new samples, while version 1.95 is used for the official CLIC samples. It was recommended by the Whizard authors to use version 1.97 as it contains a unitarisation scheme that ensures the probabilities remain physical up to high energies when considering the effect of anomalous gauge couplings.

The hadronic channels are the dominant decay modes of the W and the Z boson, with branching fractions of the order of 70% for both (REFERENCE PDG), and as the vector boson scattering is the desired signal channel, the focus of this analysis will be upon the hadronic decays of the W and Z. The vector boson scattering dominated signal final states containing hadronic decay products for the bosons are $\nu\nu\text{qqqq}$, $l\nu\text{qqqq}$ and $ll\text{qqqq}$.

2.2.1. Cross Section Sensitivity

To determine which final states are sensitive to α_4 and α_5 a comparison was made between the cross section using the standard model values of α_4 and α_5 , i.e. 0, and the same calculation using non-zero values of these couplings. This comparison was performed on all final states that would be relevant either as signal or background processes, for an analysis involving the purely hadronic decay channels of a vector boson scattering process. In full the states that were tested are:

- Vector boson scattering signal final states that are expected to show sensitivity to the anomalous couplings: $e^+e^- \rightarrow \nu\nu\text{qqqq}$, $e^+e^- \rightarrow l\nu\text{qqqq}$ and $e^+e^- \rightarrow ll\text{qqqq}$
- Four jet final states arising from e^+e^- interactions: $e^+e^- \rightarrow \text{qqqq}$.
- Two jet final states arising from e^+e^- interactions: $e^+e^- \rightarrow \nu\nu\text{qq}$, $e^+e^- \rightarrow l\nu\text{qq}$, $e^+e^- \rightarrow ll\text{qq}$ and $e^+e^- \rightarrow \text{qq}$.
- Four jet final states arising from the interactions of either e^+ or e^- with a beamstrahlung photon: $\gamma_{\text{BS}}e^- \rightarrow \text{qqqq}e^-$, $e^+\gamma_{\text{BS}} \rightarrow \text{qqqq}e^+$, $\gamma_{\text{BS}}e^- \rightarrow \text{qqqq}\nu$ and $e^+\gamma_{\text{BS}} \rightarrow \text{qqqq}\nu$.

- Four jet final states arising from the interactions of either e^+ or e^- with the electromagnetic field of the opposing beam particle. These cross sections are calculated using equivalent photon approximation (EPA), which represents the electromagnetic field of the opposing beam particle as a series of photon and so the final states appear as interactions of e^+ or e^- with photons: $\gamma_{\text{EPA}} e^- \rightarrow qqqqe^-$, $e^+ \gamma_{\text{EPA}} \rightarrow qqqqe^+$, $\gamma_{\text{EPA}} e^- \rightarrow qqqq\nu$ and $e^+ \gamma_{\text{EPA}} \rightarrow qqqq\nu$.
- Four jet final states arising from the interaction of the electromagnetic fields of opposing beam particles using the EPA approximation: $\gamma_{\text{EPA}} \gamma_{\text{EPA}} \rightarrow qqqq$.
- Four jet final states arising from the interaction of the electromagnetic field of either e^+ or e^- using the EPA approximation with a beamstrahlung photon: $\gamma_{\text{EPA}} \gamma_{\text{BS}} \rightarrow qqqq$ or $\gamma_{\text{BS}} \gamma_{\text{EPA}} \rightarrow qqqq$.
- Four jet final states arising from the interaction of two beamstrahlung photons: $\gamma_{\text{BS}} \gamma_{\text{BS}} \rightarrow qqqq$.

Note: In the above list $q = u, d, s, c$ and $b, l = e, \mu, \tau$ and $\nu = \nu_e, \nu_\mu$ and ν_τ .

The cross section was found to differ when using non-zero values for the anomalous couplings in comparison to the standard model prediction for the vector boson scattering signal final states $\nu\nu qqqq$, $l\nu qqqq$ and $ll qqqq$. The cross section comparisons for these final states can be found in table 2.1 and table 2.2 for 1.4 and 3 TeV samples respectively. In reality, non-zero anomalous couplings would change the cross sections of all processes considered, however, the sensitivity would only arise from high order terms in the Lagrangian. Such terms would not be dominant in determining the cross section and so are omitted from the generator making certain final states appear invariant to changes in the anomalous couplings.

The cross section calculations show that the most sensitive final state to the anomalous gauge couplings is $\nu\nu qqqq$, therefore, this analysis will focus solely upon this final state. Furthermore, as the $l\nu qqqq$ final state has a much reduced sensitivity in comparison to the $\nu\nu qqqq$ state and as the $ll qqqq$ can be easily vetoed from the analysis, as will be shown in subsequent chapters, it is only necessary to consider the sensitivity of the $\nu\nu qqqq$ final state. For the aforementioned reasons the $l\nu qqqq$ and $ll qqqq$ final states will be treated as backgrounds that are invariant to changes in the anomalous couplings α_4 and α_5 .

Final State	Cross Section [fb] ($\alpha_4 = \alpha_5 = 0.00$)	Cross Section [fb] ($\alpha_4 = \alpha_5 = 0.05$)	Percentage Change[%]	CLIC Cross Section [fb]
$e^+ e^- \rightarrow \nu\nu qqqq$	20.8	34.6	+66.3	24.7
$e^+ e^- \rightarrow l\nu qqqq$	112	113	+0.9	115.3
$e^+ e^- \rightarrow llqqqq$	59.7	68.6	+14.9	62.1

Table 2.1.: Cross section for selected processes for given value of α_4 and α_5 at 1.4 TeV.

Final State	Cross Section [fb] ($\alpha_4 = \alpha_5 = 0.000$)	Cross Section [fb] ($\alpha_4 = \alpha_5 = 0.005$)	Percentage Change[%]	CLIC Cross Section [fb]
$e^+ e^- \rightarrow \nu\nu qqqq$	51.2	77.7	+51.8	71.5
$e^+ e^- \rightarrow l\nu qqqq$	111.9	115.9	+3.6	106.6
$e^+ e^- \rightarrow llqqqq$	169.7	161.7	-4.9	169.3

Table 2.2.: Cross section for selected processes for given value of α_4 and α_5 at 3 TeV.

2.2.2. Anomalous Gauge Coupling Event Weights

The sensitivity of an individual event to the anomalous gauge couplings is determined through an event weight. This weight is given by the ratio of the squares of the matrix element used in the cross section calculation, one matrix element using non-zero values of α_4 and α_5 and the other matrix element using the standard model values of α_4 and α_5 , i.e. 0. The weight varies as a function of α_4 and α_5 as well as varying on an event by event basis as the kinematics of the final state changes. Examples of the event weights as a function of α_4 and α_5 for selected events is shown in figure 2.1 for 1.4 TeV events.

This reweighting procedure has many advantages over the alternative of generating new samples with fixed α_4 and α_5 , notably the absence of systematic errors arising from new event generation, simulation and reconstruction.

2.2.3. Validation of Samples

The CLIC experiment has a repository of simulated and reconstructed samples that can be used for physics analyses, however, it is not possible to calculate the event weights for these samples as the raw Whizard format event files are missing. Therefore, a new $e^+ e^- \rightarrow \nu\nu qqqq$ sample was generated with the relevant files to make reweighting as

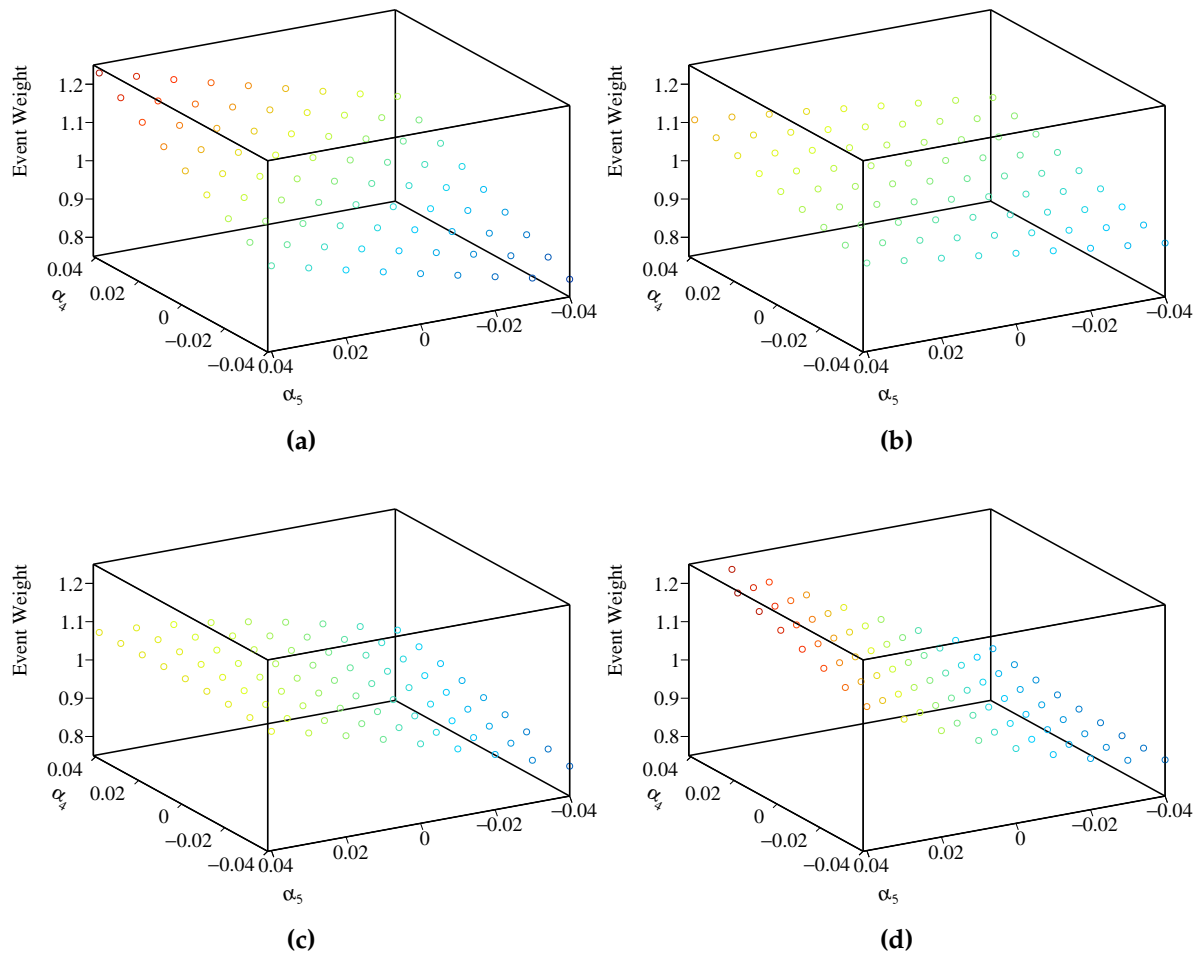


Figure 2.1.: A selection of plots showing how the event weight changes when varying the anomalous couplings α_4 and α_5 for 1.4TeV $\nu\nu\text{qqqq}$ final state events.

a function of α_4 and α_5 possible. An identical setup to that used for the production of official CLIC samples was used for the event generation, detector simulation and reconstruction. Mimicking this production chain made it possible to use the official CLIC samples for the background final states used in this analysis.

Several reconstructed level distributions were compared to the official CLIC samples and were found to be comparable to each other. A selection of these distributions is shown in figure 2.2.

In order to determine the event weights it was necessary to use the anomalous gauge coupling model in Whizard, which in turn enforces a unit CKM matrix. In the context of vector boson scattering this will restrict the hadronic decays of the W^- boson to $d\bar{u}$ and $s\bar{c}$, the W^+ boson to $u\bar{d}$ and $c\bar{s}$ and the Z boson to $u\bar{u}$, $d\bar{d}$, $s\bar{s}$, $c\bar{c}$ and $b\bar{b}$. In contrast the official CLIC samples use a non-unit CKM matrix, which gives rise to alternative hadronic decay modes for the W and Z bosons. When comparing the unit CKM matrix and the non-unit CKM $\nu\nu qqqq$ final state samples it was found that there were negligible differences in a variety of reconstructed level distributions, such as those found in figure 2.2. Furthermore, as flavour tagging information is not used in this analysis this difference was deemed insignificant.

2.3. Simulation and Reconstruction

For all samples considered in this analysis, the CLID_ILD detector [1] was used. The detector was simulated using MOKKA [10], a GEANT4 [2] wrapper providing detailed geometric descriptions of detector concepts for the linear collider. Events were reconstructed using MARLIN [5], a c++ framework designed for reconstruction at the linear collider. PandoraPFA [9, 16] is used to apply particle flow calorimetry in this reconstruction.

The CLIC_ILD is a variant of the ILD detector described in section REFERENCE. The only significant difference between the models is that CLIC_ILD has a 60 layer scintillator-tungsten HCal in comparison to the 48 layers found in the default ILD detector. The thicknesses of the layers in the HCal models are identical, so the extra layers correspond to an increase in the total thickness of the HCal. This is needed to compensate for the effects of leakage at the higher energies seen by the CLIC experiment in comparison to the ILC.

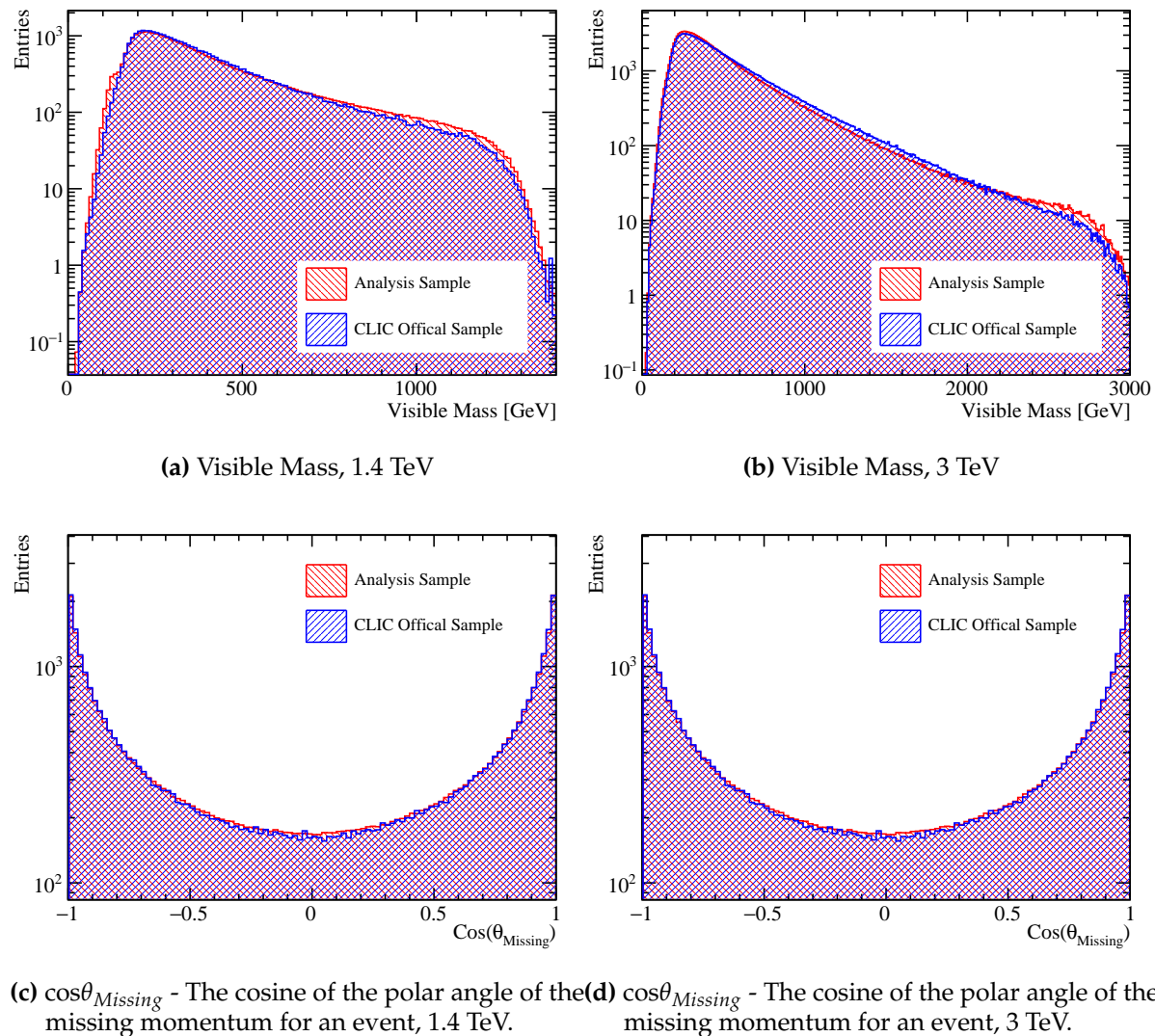


Figure 2.2.: Comparison of various distributions between samples used in this analysis and the official CLIC samples for the $\nu\nu\text{qqqq}$ final state at 1.4 and 3 TeV. Both samples have been normalised to the correct luminosity for CLIC running at the relevant energies TeV.

2.3.1. Experimental Conditions at CLIC

The CLIC experiment will operate in a unique environment in comparison to previous generations of lepton colliders and this must be properly accounted for to get an accurate measure of the physics potential that CLIC has to offer. The following aspects of the CLIC experiment present the largest challenges to the physics potential for the CLIC experiment:

- The high bunch charge density. The small beam size at the impact point produces very large electromagnetic fields. These fields can interact with the opposite beam particles causing them to radiate photons in an effect known as beamstrahlung. Beamstrahlung acts to reduce the collision energy of the e^+e^- pairs.
- Beam related backgrounds. Beamstrahlung photons can subsequently interact to produce background events that must be accounted for. Dominant backgrounds of this form that cannot be easily vetoed in the reconstruction include incoherent pair production of e^+e^- and $\gamma\gamma \rightarrow \text{Hadron}$.
- Fast readout technology is crucial. The CLIC bunch train consists of 312 bunches with a repetition rate of 50 Hz. Each bunch is separated by 0.5ns, therefore, it will be necessary to integrate over multiple bunch crossing when reading out the detectors. This places tight constraints on all detector electrical readout speeds and time resolutions.

Beam-Related Backgrounds at CLIC

The primary sources of background for the CLIC experiment are as follows:

- e^+e^- pair creation from the interaction of a beamstrahlung photons with the opposing beam. The different mechanisms for pair creation are as follows:
 - **Coherent pair production.** This mechanism involves the interaction of a real beamstrahlung photon with the electromagnetic field from the opposing beam.
 - **Trident pair production.** This mechanism involves the interaction of a virtual beamstrahlung photon with the electromagnetic field from the opposing beam.

- **Incoherent pair production.** This mechanism involves the interaction of a real or virtual beamstrahlung photon with the individual particles in the opposing beam.
- $\gamma\gamma \rightarrow \text{Hadron}$ from the interaction of real or virtual beamstrahlung photons with each other. Example Feynman diagrams for such processes is shown in figure ??.
- Beam halo muons that arise from interactions of the beam particles during collimation. The dominant mechanisms producing beam halo muons are photon conversions into muon pairs ($\gamma e^- \rightarrow \mu^+ \mu^- e^-$) and annihilation of positrons with atomic e^- into muon pairs ($e^+ e^- \rightarrow \mu^+ \mu^-$) [13].

Each of these has to be properly addressed to get a true measure of the physics potential at CLIC. Coherent and trident pair production is not a dominant source of background as they are produced at low transverse momenta, as figure 2.3 shows, and a simple cut would veto these backgrounds. This is not the case for incoherent pair production of $e^+ e^-$, which are dominant in the forward regions of the detector, and $\gamma\gamma \rightarrow \text{Hadron}$, which are dominant in the tracker and the calorimeters (with the exception of low radii in the calorimeter endcaps) [8, 14]. Beam halo muons are not a major source of background either as they can be easily removed during the reconstruction due to the clear signal they create in the detector. An algorithm was developed within the PandoraPFA framework for this purpose and it was found to be highly effective at removing the beam halo muons background [8].

$\gamma\gamma \rightarrow \text{Hadron}$ events are the most dominant source of background to consider at CLIC as these events deposit more energy throughout the detector than incoherent pair production of $e^+ e^-$ events [8]. The effect of the $\gamma\gamma \rightarrow \text{Hadron}$ background is incorporated into this analysis by overlaying $\gamma\gamma \rightarrow \text{Hadron}$ events onto the event samples used in this analysis. The overlaid backgrounds are added prior to reconstruction so that their effect on the reconstruction is fully accounted for. For a given event the exact number of background events overlaid is drawn from a Poisson distribution with a mean of 3.2 (1.3) events per bunch crossing at 3 (1.4) TeV. While incoherent pairs are still a source of background they will produce a second order effect in comparison to the $\gamma\gamma \rightarrow \text{Hadron}$ events.

The PFO choices described in section 2.6 are applied to veto the effect of PFOs that arise from the overlaid $\gamma\gamma \rightarrow \text{Hadron}$ events.

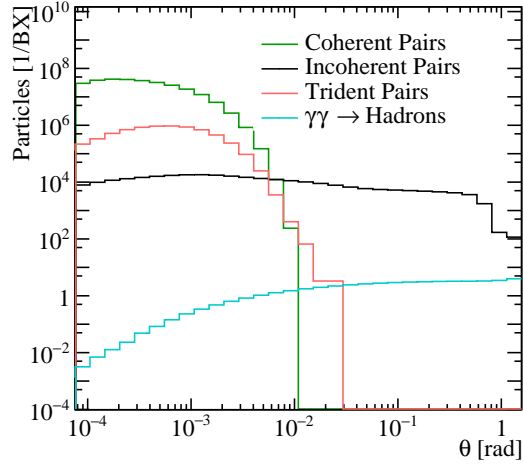


Figure 2.3.: Angular distribution of number of particles for beam induced backgrounds for CLIC at $\sqrt{s} = 3$ TeV. Taken from CLIC CDR.

2.4. Analysis

The focus of this section is to describe the post reconstruction procedure applied to the signal and background events, described in [2.2.1](#), to extract the relevant information needed for this sensitivity study.

2.4.1. Jet Pairing

The MarlinFastJet processor, a wrapper for the FastJet [4] processor, is used to cluster the signal and background events into four jets. In the case of the signal final state, $\nu\nu qqqq$, it is assumed these four jets have arisen from the hadronic decays of the bosons involved in the vector scattering process. These jets are paired up on the assumption that the correct pairing is achieved when the invariant masses of the two pairs are closest together.

The longitudinally invariant k_t jet algorithm in exclusive mode was used for the jet clustering. In contrast to the inclusive mode, the exclusive mode allows the user to request a fixed number of jets in the output from MarlinFastJet. The longitudinally invariant k_t algorithm proceeds as follows:

- For each pair of particles, i and j, the k_t distance, d_{ij} , and beam distance, $d_{iB} = p_t^2$, are calculated.

$$d_{ij} = \min(p_{ti}^2, p_{tj}^2) \Delta R_{ij}^2 / R^2 \quad (2.1)$$

where $\Delta R_{ij}^2 = (y_i - y_j)^2 + (\phi_i - \phi_j)^2$, p_t is the transverse momentum of the particle with respect to the beam axis, y_i is the rapidity of particle i and ϕ_i is the azimuthal angle of particle i. R is a configurable parameter that typically is of the order of 1.

- The minimum distance, d_{\min} , of all the k_t and beam distances is found. If the minimum occurs for a k_t distance, merge particles i and j, summing their 4-momenta in the energy combination scheme. If the beam distance is the minimum, declare particle i to be apart of the "beam" jet. Remove this particle from the list of particles and do not included in the final jet output.
- Repeat until the requested number of jets have been created, or inclusive mode no particles are left in the event.

Two other clustering algorithms were considered, but, as figure 2.4 shows, were found to be inappropriate for the experimental conditions at CLIC. These alternative algorithm choices are applied in the same manor as the longitudinally invariant k_t algorithm, however, they differ in their for the k_t distance, d_{ij} , and beam distance, d_{iB} .

The first alternative jet algorithm considered was the k_t algorithm for e^+e^- colliders (or Durham algorithm) where $d_{ij} = 2\min(E_i^2, E_j^2)(1 - \cos\theta_{ij})$ and d_{iB} is not used. θ_{ij} is the opening angle of particles i and j meaning that in the collinear limit d_{ij} corresponds to the relative transverse momenta of the particles. The major failure of this algorithm when applied to CLIC is the absence of d_{iB} , which leads to many beam related background particles being associated to jets. As figure 2.4 shows, the invariant mass of the paired jets, which is expected to be centred around the W and Z boson masses, is much larger than expected, due to the presence of the beam related backgrounds in the jets. Also this algorithm is not invariant to boosts along the beam direction making it inappropriate to use at CLIC as the beam induced backgrounds modify the nominal collision kinematics.

The second alternative jet algortihm considered was the Cambridge/Aachen jet algorithm where $d_{ij} = \Delta R_{ij}^2 / R^2$ and $d_{iB} = 1$. This algorithm gave poor performance as does not account for the transverse momentum or energy of the particles being

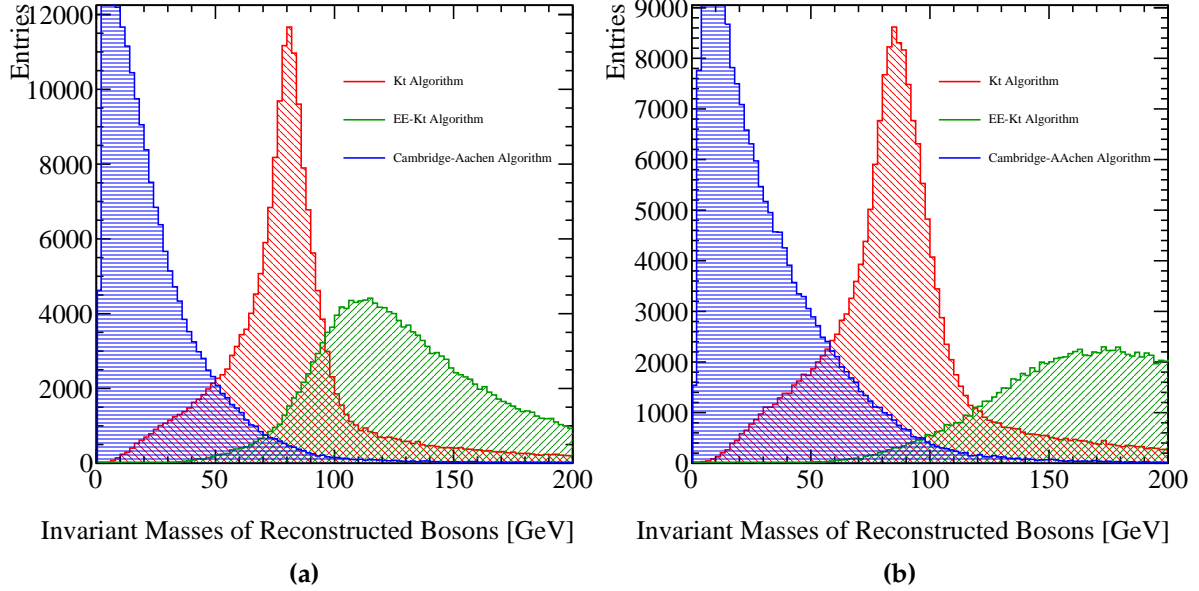


Figure 2.4.: Reconstructed masses for different choices of jet algorithm for 1.4 TeV and 3 TeV $\nu\nu\text{qqqq}$ events. These masses arise by forcing the reconstructed events into 4 jets and then pairing up the jets into pairs such that the reconstructed invariant masses of the pairs are closest to each other. These samples should be dominated by vector boson scattering involving pairs of W bosons and so it is expected that a peak at the W boson true mass should be observed. As this does not occur for the Cambridge-Aachen algorithm or the ee_kt algorithm they were deemed unsuitable for this analysis at both 1.4 and 3 TeV. In the case of the kt algorithm and the ee_kt algorithm an R parameter of 0.7 was used.

clustered. In essence, this is a cone clustering algorithm with a cone radius defined through $\Delta R_{ij} = R$, which even for large R was found to discard too much energy in the event to be useful for this analysis. This can be seen in figure 2.4 as the invariant mass of the paired jets is much lower than expected. This algorithm is useful for events with highly boosted jets, but at CLIC the jets are too disperse for this algorithm to be successfully applied.

2.4.2. Isolated Lepton Finding

Unsure of details needed in this section.

An isolated lepton finder is included in the analysis chain in an attempt to reject background events containing leptons.

2.4.3. Flavour Tagging

Don't actually use in this analysis. I assume I skip this section. The LCFIPlus [15] processor is also run on these events once clustered into jets to produce a value for the B and C tag likelihood for a jet.

This information is available for background rejection rather than contributing to the sensitivity of the event to the anomalous couplings. The LCFIPlus vertex processor was trained using events of $e^+e^- \rightarrow Z\nu\nu \rightarrow q\bar{q}\nu\nu$ for $q = u,d,s,c,b$.

2.4.4. Analysis Processor

Best way to show this?

Finally, an analysis processor is run, which calculates a number of variables used downstream in the analysis. Included in these are:

- Number of PFOs in the jets and the paired up bosons.
- Number of charged PFOs in the jets and paired up bosons.
- Highest energy PFO: energy, momentum, transverse momentum, $\cos\theta$.
- Highest energy electron PFO: energy, momentum, transverse momentum, $\cos\theta$.
- Highest energy muon PFO: energy, momentum, transverse momentum, $\cos\theta$.
- Highest energy photon PFO: energy, momentum, transverse momentum, $\cos\theta$.
- (If in existence) Highest and second highest energy isolated lepton: energy, momentum, transverse momentum, $\cos\theta$.
- Bosons: energy, momentum, transverse momentum, $\cos\theta$.
- Invariant mass of the boson pair.
- Jets: energy, momentum, transverse momentum, $\cos\theta$.
- $\cos\theta$ Of the missing 3-momentum vector.
- Recoil mass.
- Invariant mass of the visible system.

- y_i, y_{i+1} . Jet clustering parameters ranging from $i = 0$ to 6.
- $\text{Cos}\theta_{jet}^*$. This is the opening angle of a pair of jets, assumed to be from a signle boson, in the rest frame of the boson.
- $\text{Cos}\theta_{Boson}^*$. This is the opening angle of a pair of bosons, assumed to be from vector boson scattering, in the rest frame of the di-boson pair.
- Transverse momentum and energy of the event.
- Acolinearity of the jet pairs forming the bosons and the acoilinearity of the boson pair.
- Principle thrust T and the thrust axes $\bar{\mathbf{n}}$. Note $\bar{\mathbf{n}}$ is a unit vector. These are defined by the following equation

$$T = \max_{\bar{\mathbf{n}}} \left(\frac{\sum_i \mathbf{p}_i \cdot \bar{\mathbf{n}}}{\sum_i |\mathbf{p}_i|^2} \right) \quad (2.2)$$

- The major and minor thrust values. These are defined with respect to the thrust axes $\bar{\mathbf{n}}$ in the following way:

$$T = \max_{\bar{\mathbf{n}}_{major}} \left(\frac{\sum_i \mathbf{p}_i \cdot \bar{\mathbf{n}}_{major}}{\sum_i |\mathbf{p}_i|^2} \right) \quad (2.3)$$

where $\bar{\mathbf{n}}_{major} \cdot \bar{\mathbf{n}} = \mathbf{0}$. Similarly the minor thrust value is defined as

$$T = \frac{\sum_i \mathbf{p}_i \cdot \bar{\mathbf{n}}_{minor}}{\sum_i |\mathbf{p}_i|^2} \quad (2.4)$$

where $\bar{\mathbf{n}}_{minor} \cdot \bar{\mathbf{n}} = \bar{\mathbf{n}}_{minor} \cdot \bar{\mathbf{n}}_{major} = \mathbf{0}$

- Sphericity. This is defined using the sphericity tensor S^{ab} defined as:

$$S^{ab} = \frac{\sum_i p_i^\alpha p_j^\alpha}{\sum_{i,\alpha=1,2,3} |p_i^\alpha|^2} \quad (2.5)$$

Where p_i are the components of the momenta of particle i in the frame of the detector and the sum runs over all particles in the event. Sphericity is defined as $S = \frac{3}{2}(\lambda_2 + \lambda_3)$, where λ_i are the eigenvalues of the sphericity tensor defined such $\lambda_1 \geq \lambda_2 \geq \lambda_3$. This provides a measure of how spherical the reconstructed

event topology is with isotropic events having $S \approx 1$, while two jet events have $S \approx 0$. (Also $\lambda_1 + \lambda_2 + \lambda_3 = 1$.)

- Aplanarity. Aplanarity is defined as $\frac{3}{2}\lambda_3$ where λ_3 is an eigenvalue of the sphericity tensor. This provides a measure of whether an event is linear or planar.
- B and C tag values for the jets, the min and max B and C tag values for the bosons.

Alongside these variables, for the $\nu\nu\text{qqqq}$ final state a number of Monte-Carlo variables are calculated for informative purposes and are not used in the analysis. These include:

- The quark and neutrino 4 momenta.
- Invariant mass of boson pair using MC pairing and MC energy.
- Invariant mass of boson pair using MC pairing and reconstructed jet energy.

2.5. Fitting Technique

The metric used to determine the optimal jet algorithm for this analysis is the sensitivity of the pure signal final state, $\nu\nu\text{qqqq}$, to the anomalous gauge couplings. Pure signal was used in the optimisation to avoid the need to process the large number of background files for each iteration of the jet algorithm considered, while still basing the optimisation on the physics of interest. The focus of this section in the description of the fitting technique that will be used for both jet algorithm optimisation and in the final sensitivity study.

2.5.1. Choice of Fitting Distribution

The sensitivity of CLIC to the anomalous gauge couplings is determined through the use of a χ^2 fit to the distribution of $\cos\theta_{\text{jets}}^*$. For a given event, the jet clustering and pairing proceeds as described in section 2.4 and leads to the event being clustered into four jets, which are then paired up to give two candidate bosons. θ_{jets}^* is defined as the opening angle of the jets in the rest frame of these candidate bosons. The distribution of $\cos\theta_{\text{jets}}^*$ proved to be highly sensitive to the anomalous gauge couplings as shown in figure 2.5.

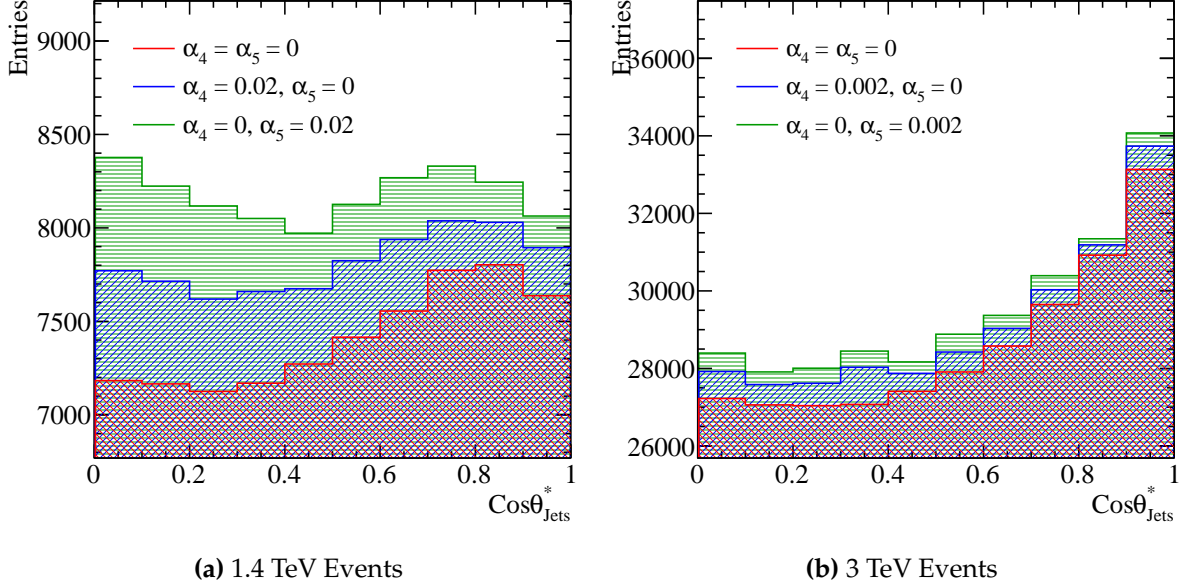


Figure 2.5.: Sensitivity of $\cos\theta_{\text{jets}}^*$ to anomalous couplings at 1.4 and 3 TeV. The jet algorithm used for this example was the longitudinally invariant k_t algorithm with an R parameter of 0.7. This sample corresponds to pure signal of hadronic decays in vector boson scattering i.e. $\nu\nu qqqq$.

The distribution of $\cos\theta_{\text{Bosons}}^*$ was also considered for this sensitivity study, however, it proved to be less sensitive than $\cos\theta_{\text{jets}}^*$. This can be seen when comparing figures 2.5 and 2.6. θ_{Bosons}^* is defined as the opening angle between the two candidate bosons two bosons in the rest frame of the candidate boson pair. Furthermore, it was found that the χ^2 distribution formed from the two dimensional distribution of $\cos\theta_{\text{jets}}^*$ against $\cos\theta_{\text{Bosons}}^*$ did not significantly benefit the sensitivity in comparison using the one dimensional distribution of $\cos\theta_{\text{jets}}^*$ and therefore was not considered for this analysis.

2.5.2. Application Of Anomalous Gauge Coupling Event Weights

As described in section 2.2.2, event weights are used to determine the sensitivity of CLIC to the anomalous gauge couplings. These event weights are extracted on an event by event basis for the signal final state $\nu\nu qqqq$ from the generator software Whizard. To achieve a smooth χ^2 distribution in the final result a fine sampling of the $\cos\theta_{\text{jets}}^*$ distribution in the α_4 and α_5 space is needed, however, extracting the weights on an event by event basis to populate this distribution is highly CPU intensive. While this is feasible, it is highly impractical and so in an attempt to resolve this issue, an

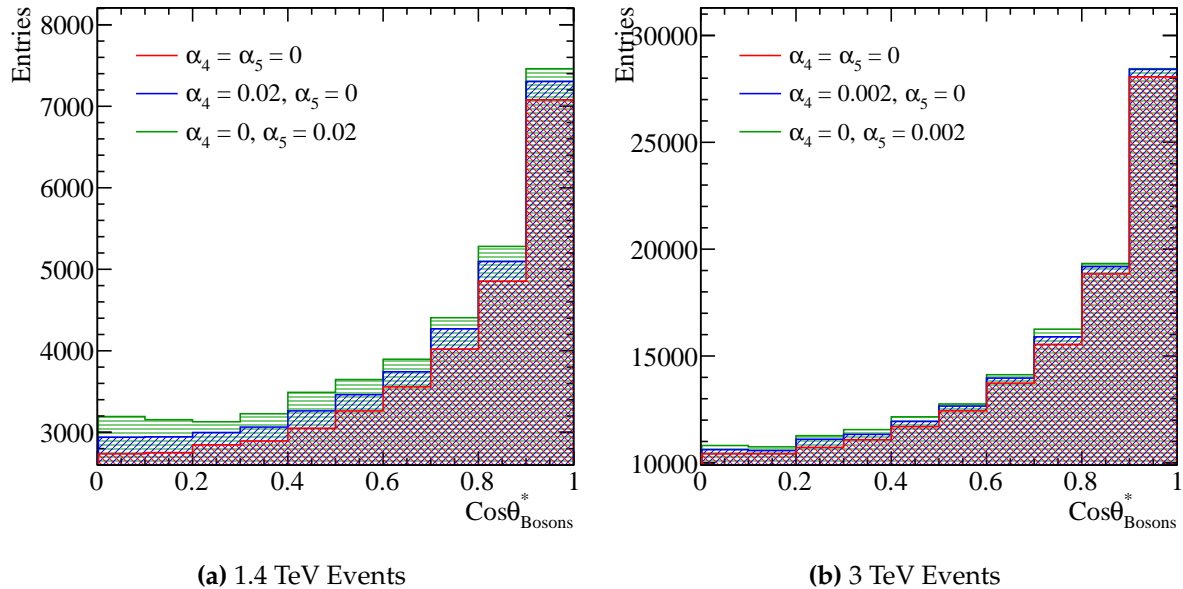


Figure 2.6.: Sensitivity of $\cos\theta_{Bosons}^*$ to anomalous couplings at 1.4 and 3 TeV. The jet algorithm used for this example was the longitudinally invariant kt algorithm with an R parameter of 0.7. This sample corresponds to pure signal of hadronic decays in vector boson scattering i.e. $\nu\nu\text{qqqq}$.

interpolation scheme was applied to determine the event weights within a sampled region of the α_4 and α_5 space. This allows for an infinite sampling of the $\cos\theta_{Jets}^*$ distribution in the space of α_4 and α_5 within the sampled region, without having to call the generator an infinite number of times.

A bicubic interpolation scheme, cubic interpolation along two dimensions, was applied to the event weights that were extracted from the generator. This procedure is best illustrated by showing the interpolated surface superimposed with the raw event weights from the generator, which is shown for several $\nu\nu\text{qqqq}$ events at 1.4 TeV in figure 2.7 (ADD 3 TEV). This interpolation scheme produces a smooth and continuous surface that is sufficiently accurate for the fitting procedure applied in this analysis.

For reference at 1.4 TeV event weights were produced from Whizard stepping along α_4 and α_5 in steps of 0.01 ranging from -0.07 to 0.07, as shown in figure 2.1, while at 3 TeC event weights were samples in steps of 0.00025 from -0.0045 to 0.0045. These ranges proved to be sufficient for the contours of interest for the CLIC sensitivity analysis at this energy.

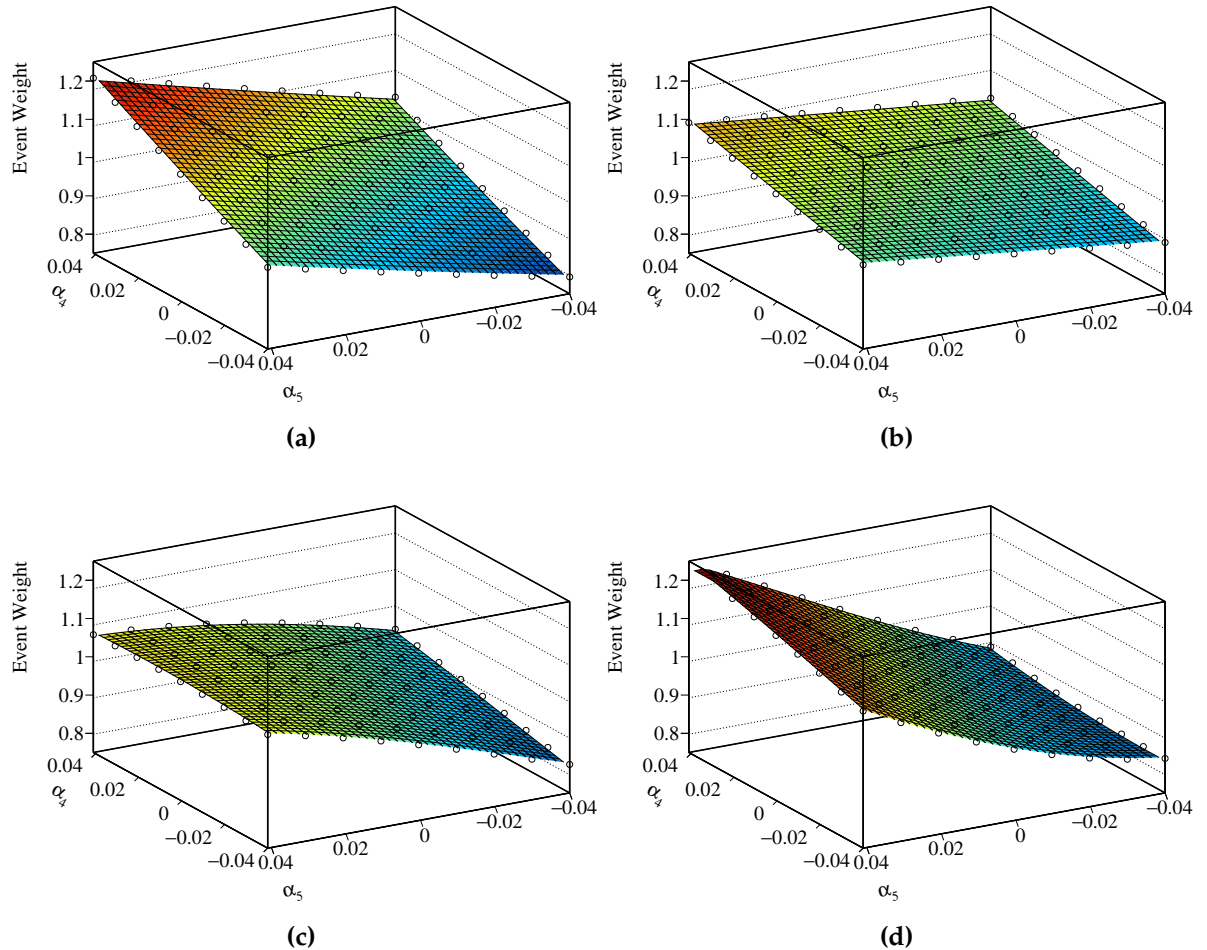


Figure 2.7.: A selection of plots showing how the event weight changes when varying the anomalous couplings α_4 and α_5 for 1.4TeV $\nu\nu\text{qqqq}$ final state events. The hollow circles show the event weight produced from the generator while the surface shown is found using bicubic interpolation between those points.

2.5.3. Analysis of Fitting Distribution

The $\cos\theta_{Jets}^*$ variable was binned in a histograms containing 10 bins before begin converted into a value of χ^2 . This binning was selected to maximise the number of bins in the distribution, while minimising the effect of large bin by bin fluctuations arising from individual events with large event weights.

Using these interpolated surfaces for the event weights, distribution of $\cos\theta_{Jets}^*$ were produced stepping across α_4 and α_5 in steps of 0.0001 at 1.4 TeV and 0.00001 at 3 TeV. Each distribution was converted into a value of χ^2 using the following formula:

$$\chi^2 = \sum_i \frac{(O_i - E_i)^2}{E_i} \quad (2.6)$$

where O_i is the observed bin content for bin i in the distribution with non-zero α_4 and α_5 and E_i is the expected bin content for bin i in the distribution with zero α_4 and α_5 i.e. the standard model expected value.

Confidence limits indicate the probability of measuring a given value of χ^2 in the α_4 and α_5 space. The confidence limits used in subsequent sections, 68%, 90% and 99% are defined using constant χ^2 contours of 2.28, 4.61 and 9.21, which arise from the integral of the two dimensional χ^2 function.

It is useful to reduce these distributions to sensitivities to the individual parameters α_4 and α_5 independently. This is done by projecting out either the $\alpha_4 = 0$ or $\alpha_5 = 0$ one dimensional χ^2 distribution from the two dimensional χ^2 distribution. Using these one dimensional plots it is possible to extract the sensitivity to an individual parameters using confidence limits arising from the integral of the two dimensional χ^2 function i.e. 68% confidence limit occurs for $\chi^2 = 0.989$. In subsequent chapters these are the sensitivities quoted for individual anomalous gauge coupling parameters.

2.6. Optimisation of Jet Reconstruction

The jet algorithm used for this analysis is the longitudinally invariant kt algorithm as described in section 2.4.1. The parameter choices under consideration for optimisation are the R parameter, used in the kt algorithm definition, used and the PFO selection.

A number of cuts [9] are applied to the transverse momenta and the time of the PFOs produced by PandoraPFA to reduce the PFOs into a subset that are believed to originate from the desired interaction in an attempt to veto the overlaid $\gamma\gamma \rightarrow$ Hadron background events. Different options for these cuts give rise to the tight, default and loose selected PFOs that are considered in this optimisation.

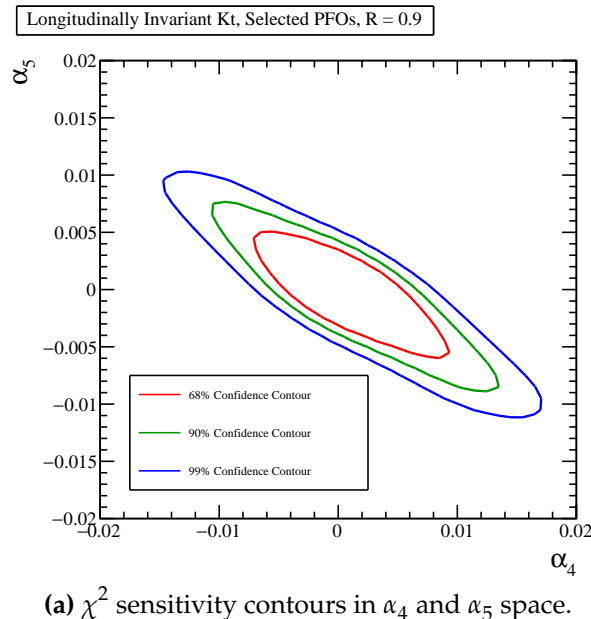
2.6.1. 1.4 TeV Optimal Jet Reconstruction

At 1.4 TeV the optimal sensitivity is achieved for either loose selected PFOs with an R parameter of 0.7 or default selected PFOs with an R parameter of 0.9 as can be seen from tables 2.3 and 2.4. As a tie breaker between these options the separation power, the fraction of events misidentified as either arising from a WW pair or a ZZ pair, was considered. Again performance was similar, but there was a slight preference towards the use of selected PFOs and an R parameter of 0.9. While not used in the primary analysis the separation of samples into WW and ZZ events is important for an extension analysis found in section BLAH.

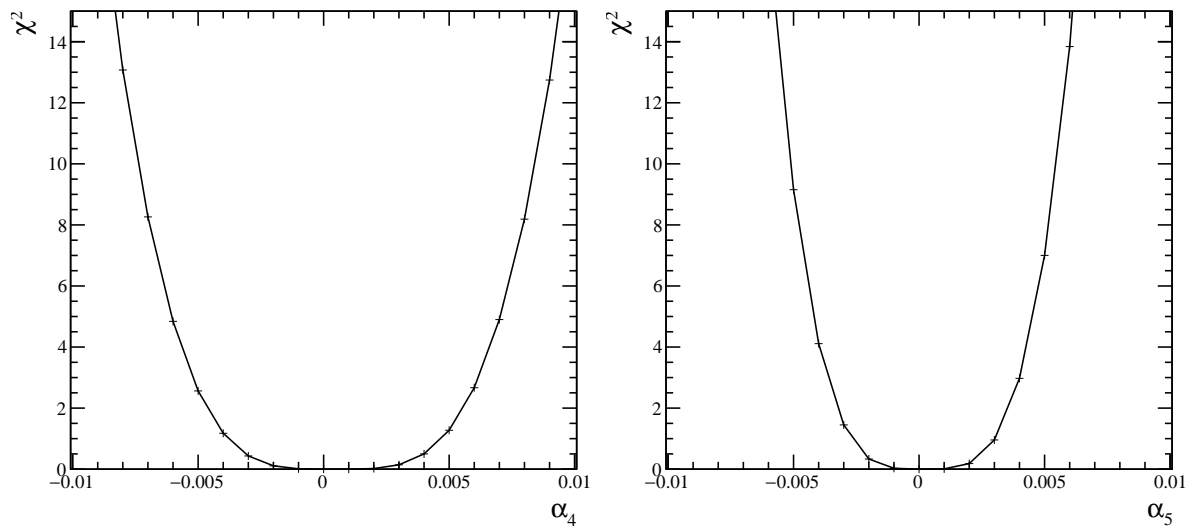
The optimal contours can be found in figure 2.8a and the optimal 1D plot used to produce the errors references in the tables 2.3 and 2.4 can be found in figures 2.8b and 2.8c respectively. All other contours and plots for this optimisation can be found in the appendices. There are minimal performance differences between the various jet algorithm configurations at 1.4 TeV.

2.6.2. 3 TeV Optimal Jet Reconstruction

At 3 TeV the optimal sensitivity for the reconstructions considered is achieved for tight selected PFOs with an R parameter of 1.1 as can be seen from tables 2.5 and 2.6. The optimal contours can be found in figure 2.9a and the optimal 1D plot used to produce



(a) χ^2 sensitivity contours in α_4 and α_5 space.



(b) χ^2 as a function of α_4 assuming $\alpha_5 = 0$.

(c) χ^2 as a function of α_5 assuming $\alpha_4 = 0$.

Figure 2.8.: χ^2 sensitivity distributions for the $qqqq\nu\nu$ final state arising from a fit to $\cos\theta_{\text{jets}}^*$ at 1.4 TeV for the optimal jet reconstruction parameters.

PFO Selection R Parameter	Tight Selected PFOs	Selected PFOs	Loose Selected PFOs
0.7	$-0.0039 + 0.0050$	$-0.0038 + 0.0050$	$-0.0037 + 0.0046$
0.9	$-0.0041 + 0.0051$	$-0.0038 + 0.0046$	$-0.0038 + 0.0048$
1.1	$-0.0041 + 0.0051$	$-0.0039 + 0.0050$	$-0.0040 + 0.0050$

Table 2.3.: Precision on measurement of α_4 at 1.4 TeV for different jet reconstruction parameters considering pure signal and applying a χ^2 fit to $\cos\theta_{Jets}^*$.

PFO Selection R Parameter	Tight Selected PFOs	Selected PFOs	Loose Selected PFOs
0.7	$-0.0027 + 0.0031$	$-0.0027 + 0.0032$	$-0.0025 + 0.0030$
0.9	$-0.0028 + 0.0032$	$-0.0026 + 0.0030$	$-0.0026 + 0.0030$
1.1	$-0.0028 + 0.0032$	$-0.0027 + 0.0032$	$-0.0028 + 0.0031$

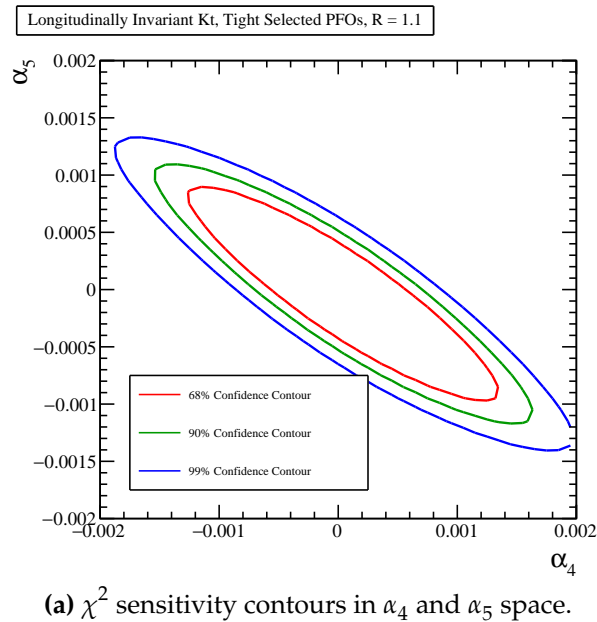
Table 2.4.: Precision on measurement of α_5 at 1.4 TeV for different jet reconstruction parameters considering pure signal and applying a χ^2 fit to $\cos\theta_{Jets}^*$.

the errors references in the tables 2.5 and 2.6 can be found in figures 2.9b and 2.9c respectively. All other contours and plots for this optimisation can be found in the appendices.

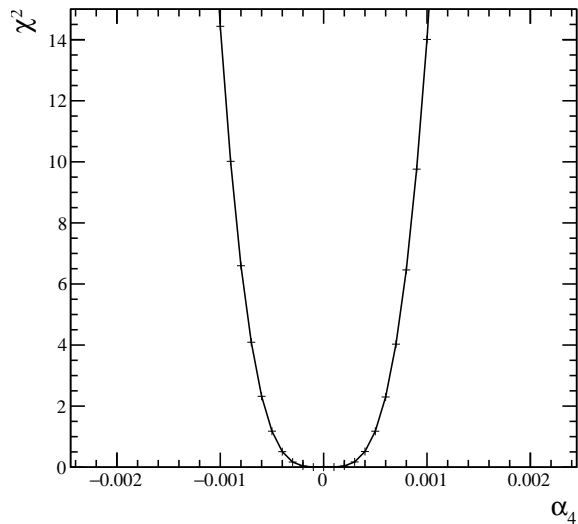
The gains in optimising the jet algorithm at 3 TeV are larger than those found at 1.4 TeV. The preference for the tight selected PFOs is to be expected as this configuration minimises the effect of beam induced backgrounds, which are more prominent at higher energies.

PFO Selection R Parameter	Tight Selected PFOs	Selected PFOs	Loose Selected PFOs
0.7	$-0.000529 + 0.000525$	$-0.000510 + 0.000507$	$-0.000547 + 0.000555$
0.9	$-0.000566 + 0.000555$	$-0.000539 + 0.000520$	$-0.000568 + 0.000553$
1.1	$-0.000472 + 0.000472$	$-0.000508 + 0.000492$	$-0.000504 + 0.000489$

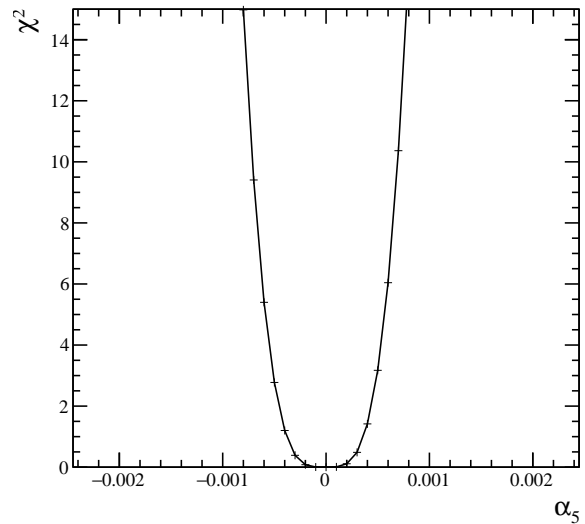
Table 2.5.: Precision on measurement of α_4 at 3 TeV for different jet reconstruction parameters considering pure signal and applying a χ^2 fit to $\cos\theta_{Jets}^*$.



(a) χ^2 sensitivity contours in α_4 and α_5 space.



(b) χ^2 as a function of α_4 assuming $\alpha_5 = 0$.



(c) χ^2 as a function of α_5 assuming $\alpha_4 = 0$.

Figure 2.9.: χ^2 sensitivity distributions for the qqqqvv final state arising from a fit to $\cos\theta_{\text{jets}}^*$ at 3 TeV for the optimal jet reconstruction parameters.

PFO Selection	Tight Selected PFOs	Selected PFOs	Loose Selected PFOs
R Parameter			
0.7	$-0.000392 + 0.000369$	$-0.000355 + 0.000348$	$-0.000356 + 0.000348$
0.9	$-0.000394 + 0.000365$	$-0.000391 + 0.000361$	$-0.000395 + 0.000368$
1.1	$-0.000350 + 0.000337$	$-0.000374 + 0.000354$	$-0.000352 + 0.000336$

Table 2.6.: Precision on measurement of α_5 at 3 TeV for different jet reconstruction parameters considering pure signal and applying a χ^2 fit to $\cos\theta_{J\ell}^*$.

2.7. Event Selection

As discussed earlier the signal events for this analysis contain the $\nu\nu\text{qqqq}$ final state. The processes to be considered in this analysis alongside the signal are events that would topologically look similar to signal in the detector. This includes events that could be confused with 4 jet events with missing energy, while excluding those events with large numbers of high energy leptons that could be vetoed easily during the analysis stage. In full the list includes:

Equivalent Photon Approximation (EPA) processes model the electromagnetic field of a charged particle as virtual photons. BS (beamstrahlung) processes involve photons that have been radiated from incoming charged particles due to interactions with the electromagnetic field of the opposite beam. The energy spectrum of the incoming particles for CLIC at the relevant operating energy is used to model the energy of these incoming photons. Included in this study are photon-photon interactions from photons appearing from the EPA and beamstrahlung processes.

2.7.1. Pre Selection - 1.4 TeV

The primary selection of the $\nu\nu\text{qqqq}$ signal will be done using a multivariate analysis, however, in an attempt to veto trivial backgrounds a simple cut based preselection is applied. Cuts are applied to the transverse momentum, invariant mass of the visible system and the number of isolated leptons. The raw distributions of these variables is shown in figure 2.10. Based on these distributions the following cuts were applied:

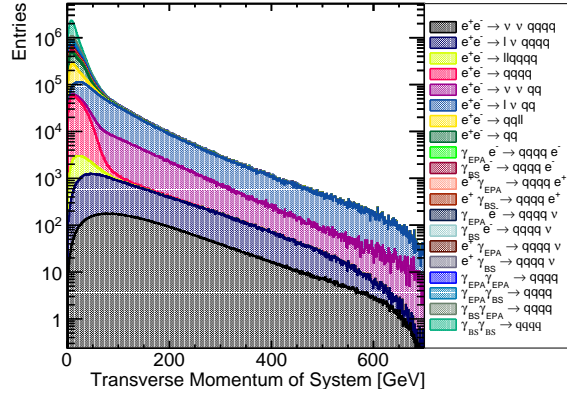
- Transverse momentum > 100 GeV. This cut is effective due to the presence of missing energy in the form of neutrinos in the signal final state.

Final State	Cross Section 1.4 TeV [fb]	Cross Section 3 TeV [fb]
$e^+ e^- \rightarrow \nu\nu qqqq$	24.7	71.5
$e^+ e^- \rightarrow l\nu qqqq$	110.4	106.6
$e^+ e^- \rightarrow llqqqq$	62.1	169.3
$e^+ e^- \rightarrow qqqq$	1245.1	546.5
$e^+ e^- \rightarrow \nu\nu qq$	787.7	1317.5
$e^+ e^- \rightarrow l\nu qq$	4309.7	5560.9
$e^+ e^- \rightarrow llqq$	2725.8	3319.6
$e^+ e^- \rightarrow qq$	4009.5	2948.9
$\gamma_{\text{EPA}} e^- \rightarrow qqqqe^-$	287.1	287.8
$\gamma_{\text{BS}} e^- \rightarrow qqqqe^-$	1160.7	1268.6
$e^+ \gamma_{\text{EPA}} \rightarrow qqqqe^+$	286.9	287.8
$e^+ \gamma_{\text{BS}} \rightarrow qqqqe^+$	1156.3	1267.3
$\gamma_{\text{EPA}} e^- \rightarrow qqqq\nu$	32.6	54.2
$\gamma_{\text{BS}} e^- \rightarrow qqqq\nu$	136.9	262.5
$e^+ \gamma_{\text{EPA}} \rightarrow qqqq\nu$	32.6	54.2
$e^+ \gamma_{\text{BS}} \rightarrow qqqq\nu$	136.4	262.3
$\gamma_{\text{EPA}} \gamma_{\text{EPA}} \rightarrow qqqq$	753.0	402.7
$\gamma_{\text{EPA}} \gamma_{\text{BS}} \rightarrow qqqq$	4034.8	2423.1
$\gamma_{\text{BS}} \gamma_{\text{EPA}} \rightarrow qqqq$	4018.7	2420.6
$\gamma_{\text{BS}} \gamma_{\text{BS}} \rightarrow qqqq$	21406.2	13050.3

Table 2.7.: Cross sections of signal and background processes at 1.4 and 3 TeV. In the above table $q \in u, \bar{u}, d, \bar{d}, s, \bar{s}, c, \bar{c}, b$ or \bar{b} while $l \in e^\pm, \mu^\pm$ or τ^\pm and $\nu \in \nu_e, \nu_\mu$ and ν_τ . The subscript EPA or BS for the incoming photons indicate whether the photon is generated from the equivalent photon approximation or beamstrahlung.

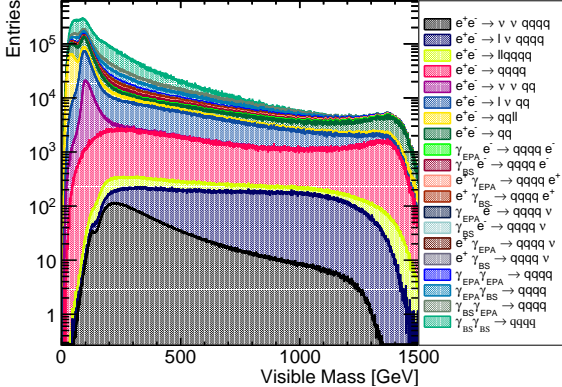
- Visible mass of the system > 200 GeV. This cut is effective for accounting for the missing energy of the neutrinos in the final state along the longitudinal direction of the detector instead.
- Number of isolated leptons = 0. This cut vetoes a large number of events with leptons in the final state. The effect of these preselection cuts can be found in table 1.3. While a large fraction of the signal events are lost through these cuts, particularly the transverse momentum cuts, a much large fraction of background events are removed justifying the cut.

(a)

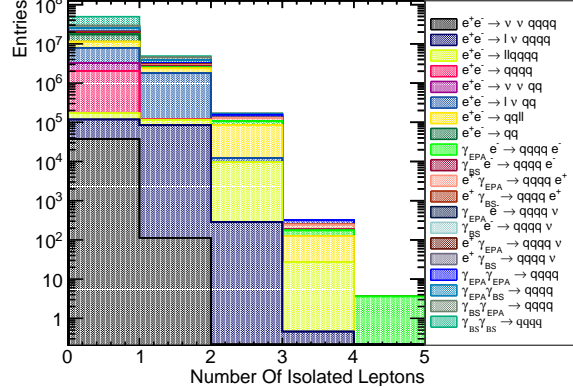


(a) Transverse momentum of system.

(b)



(b) Invariant mass of the visible system.



(c) Number of isolated leptons.

Figure 2.10.: Distribution of variables cut on in the preselection at 1.4 TeV.

The event numbers for the signal and background are shown in table 2.8 as these cuts are cumulatively applied. These numbers are normalised to the correct luminosity for CLIC running at 1.4 TeV. As is expected the large transverse momentum cut removes practically all backgrounds containing no missing energy. The invariant mass cut removes significant fractions of two quark and missing energy events. Finally, the isolated lepton finder cut removes backgrounds containing visible leptonic final states.

2.7.2. MVA - 1.4 TeV

A multivariate analysis was applied to the data set to refine the selection using the TMVA toolkit [6]. The following variables were used for training the TMVA selection.

- Number of PFOs in the event.

Final State	Raw Event Numbers	$p_T > 100 \text{ GeV}$	$p_T > 100 \text{ GeV} \& M_{\text{Vis}} > 200 \text{ GeV}$	$p_T > 100 \text{ GeV} \& M_{\text{Vis}} > 200 \text{ GeV} \& N_{\text{Isolated Leptons}} = 0$
$e^+ e^- \rightarrow \nu\nu qqqq$	37,050	23,800	21,080	21,020
$e^+ e^- \rightarrow l\nu qqqq$	165,600	81,620	80,840	42,410
$e^+ e^- \rightarrow llqqqq$	93,150	1,151	1,140	700
$e^+ e^- \rightarrow qqqq$	1,868,000	6,487	6,467	6,445
$e^+ e^- \rightarrow \nu\nu qq$	1,181,000	514,100	50,260	50,150
$e^+ e^- \rightarrow l\nu qq$	6,464,000	2,003,000	1,259,000	567,600
$e^+ e^- \rightarrow llqq$	4,088,000	7,754	7,351	5,643
$e^+ e^- \rightarrow qq$	6,011,000	34,610	34,130	34,070
$\gamma_{\text{EPA}} e^- \rightarrow qqqqe^-$	430,600	2,463	2,446	865
$\gamma_{\text{BS}} e^- \rightarrow qqqqe^-$	1,306,000	1,382	1,340	1,002
$e^+ \gamma_{\text{EPA}} \rightarrow qqqqe^+$	430,300	2,846	2,823	1,121
$e^+ \gamma_{\text{BS}} \rightarrow qqqqe^+$	1,301,000	654	643	469
$\gamma_{\text{EPA}} e^- \rightarrow qqqq\nu$	48,890	17,450	13,490	8,852
$\gamma_{\text{BS}} e^- \rightarrow qqqq\nu$	154,000	56,380	36,350	35,900
$e^+ \gamma_{\text{EPA}} \rightarrow qqqq\nu$	48,890	17,520	13,550	8,928
$e^+ \gamma_{\text{BS}} \rightarrow qqqq\nu$	153,400	56,280	36,340	35,900
$\gamma_{\text{EPA}} \gamma_{\text{EPA}} \rightarrow qqqq$	1,129,000	3,160	3,079	1,563
$\gamma_{\text{EPA}} \gamma_{\text{BS}} \rightarrow qqqq$	4,539,000	5,325	5,270	3,987
$\gamma_{\text{BS}} \gamma_{\text{EPA}} \rightarrow qqqq$	4,521,000	3,810	3,730	2,318
$\gamma_{\text{BS}} \gamma_{\text{BS}} \rightarrow qqqq$	20,550,000	2,445	2,445	1,673

Table 2.8.: Number of events passing the various cuts applied in the preselection at 1.4 TeV.

Event numbers are normalised to the correct luminosity for CLIC at 1.4 TeV. p_T is the transverse momentum of the event, M_{Vis} is the visible mass and $N_{\text{Isolated Leptons}}$ is the number of isolated leptons in the event. In the above table $q \in u, \bar{u}, d, \bar{d}, s, \bar{s}, c, \bar{c}, b$ or \bar{b} while $l \in e^\pm, \mu^\pm$ or τ^\pm and $\nu \in \nu_e, \nu_\mu$ and ν_τ . The subscript EPA or BS for the incoming photons indicate whether the photon is generated from the equivalent photon approximation or beamstrahlung.

- Highest energy PFO type.
- Transverse momentum of the event.
- $\cos\theta_{\text{Missing}}$. The cosine of the polar angle of the missing momentum.

- $\cos\theta_{\text{Highest Energy Track}}$. The cosine of the polar angle of the track with the largest momentum.
- y_i, y_{i+1} . Jet clustering parameters ranging from $i = 0$ to 6.
- Principle thrust, sphericity and aplanarity as defined in section BLAH.
- Energy of the highest energy electron in the event.
- Energy of the highest energy PFO in the event.
- Energy of the reconstructed bosons.
- Acolinearity of the reconstructed boson pair.
- Invariant mass of the reconstructed bosons.
- Acolinearity of the jets forming the reconstructed bosons.

It was found that the best MVA algorithm for both performance and speed was the booted decision tree (BDT) when comparing different methods using the default settings. Add plot here.

The BDT was further optimised by varying the number of trees used, the depth of the trees and the number of cuts applied. The results shown in the rest of this section use the optimal configuration. For the optimal BDT configuration a significance of $S/\sqrt{(S+B)} = 53.6$ was obtained.

The event numbers passing the BDT cut can be found in table 2.9. The performance of the BDT is shown in figure 2.11, which shows the change in the distribution of the invariant mass of the reconstructed bosons as the MVA is applied. As expected the dominant background processes after the MVA is applied are those that will look identical to the visible signal process i.e. $qqqq$ and missing energy. Two smaller sources of background that pass the MVA exists, those where two jets and missing energy are confused as four jets and missing energy and those where a lepton is not properly reconstructed and the events look like four jets and missing energy.

The summary of the selection procedure is given in table 2.10.

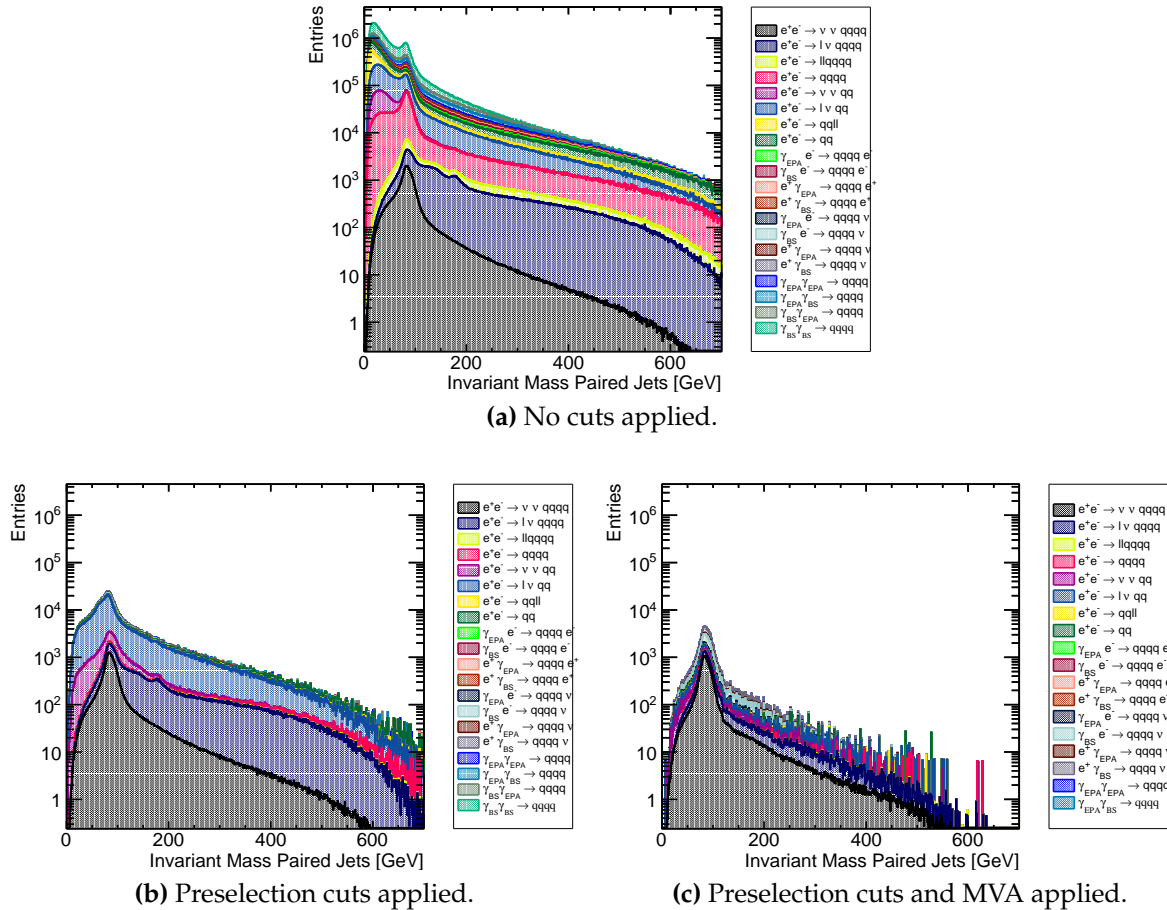


Figure 2.11.: Impact of preselection and MVA on the reconstructed invariant mass of the bosons arising from jet pairing at 1.4 TeV.

Final State	Raw Event Numbers	Post MVA Selection Numbers
$e^+e^- \rightarrow \nu\nuqqqq$	37,050	14,770
$e^+e^- \rightarrow l\nuqqqq$	165,600	6,159
$e^+e^- \rightarrow llqqqq$	93,150	80
$e^+e^- \rightarrow qqqq$	1,868,000	1,264
$e^+e^- \rightarrow \nu\nu qq$	1,181,000	3,286
$e^+e^- \rightarrow l\nu qq$	6,464,000	6,262
$e^+e^- \rightarrow ll qq$	4,088,000	234
$e^+e^- \rightarrow qq$	6,011,000	1,016
$\gamma_{\text{EPA}} e^- \rightarrow qqqqe^-$	430,300	20
$\gamma_{\text{BS}} e^- \rightarrow qqqqe^-$	1,306,000	42
$e^+ \gamma_{\text{EPA}} \rightarrow qqqqe^+$	430,300	19
$e^+ \gamma_{\text{BS}} \rightarrow qqqqe^+$	1,301,000	44
$\gamma_{\text{EPA}} e^- \rightarrow qqqq\nu$	48,890	3,552
$\gamma_{\text{BS}} e^- \rightarrow qqqq\nu$	154,000	18,540
$e^+ \gamma_{\text{EPA}} \rightarrow qqqq\nu$	48,890	3,652
$e^+ \gamma_{\text{BS}} \rightarrow qqqq\nu$	153,400	18,770
$\gamma_{\text{EPA}} \gamma_{\text{EPA}} \rightarrow qqqq$	1,129,000	68
$\gamma_{\text{EPA}} \gamma_{\text{BS}} \rightarrow qqqq$	4,539,000	55
$\gamma_{\text{BS}} \gamma_{\text{EPA}} \rightarrow qqqq$	4,521,000	0
$\gamma_{\text{BS}} \gamma_{\text{BS}} \rightarrow qqqq$	20,550,000	0

Table 2.9.: Number of events passing the MVA selection at 1.4 TeV. Event numbers are normalised to the correct luminosity for CLIC at 1.4 TeV. The subscript EPA or BS for the incoming photons indicate whether the photon is generated from the equivalent photon approximation or beamstrahlung.

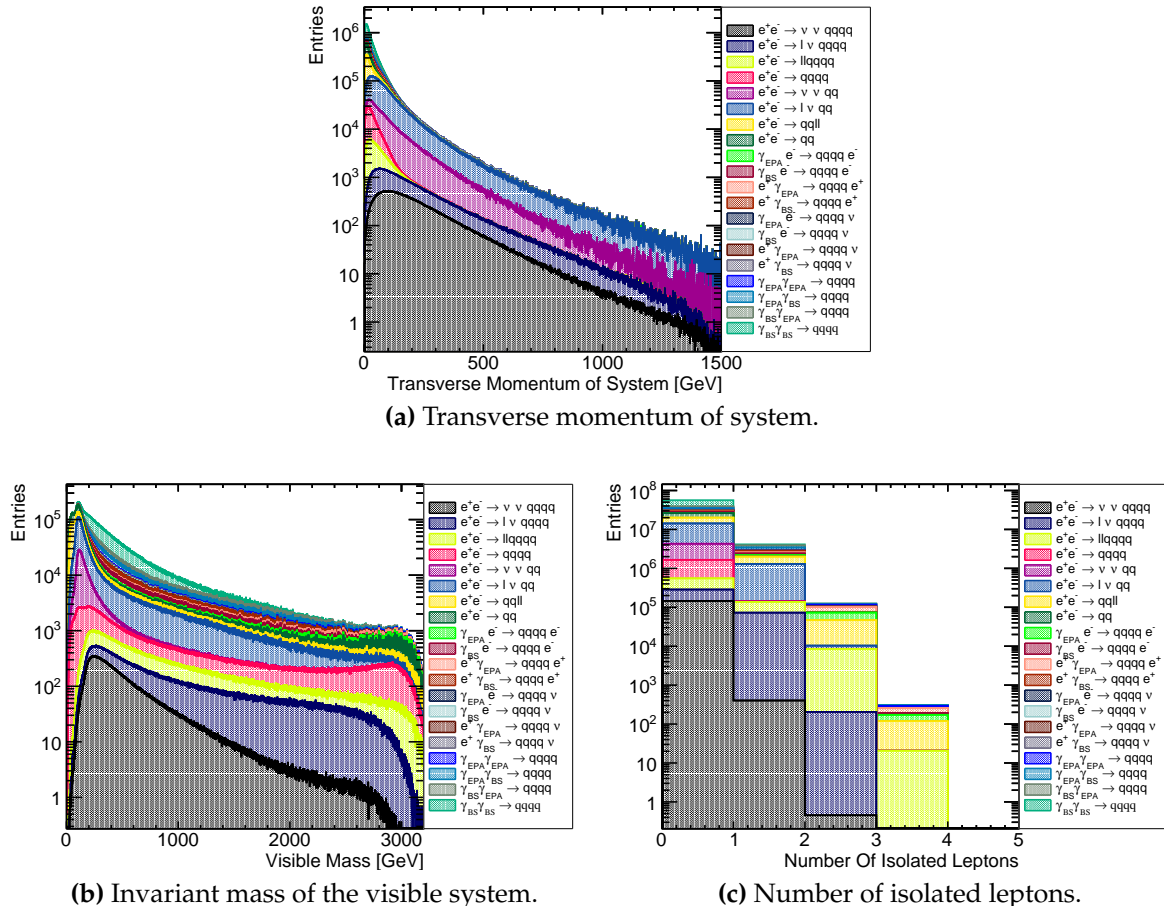


Figure 2.12.: Distribution of variables cut on in the preselection at 3 TeV.

Final State	ϵ_{presel}	ϵ_{BDT}	N_{BDT}
$e^+ e^- \rightarrow \nu\nu qqqq$	56.7%	39.9%	14,770
$e^+ e^- \rightarrow l\nu qqqq$	25.7%	3.7%	6,159
$e^+ e^- \rightarrow \nu\nu qq$	4.3%	0.3%	3,286
$e^+ e^- \rightarrow l\nu qq$	8.8%	0.1%	6,262
$\gamma_{\text{EPA}} e^- \rightarrow qqqq\nu$	18.0%	7.3%	3,552
$\gamma_{\text{BS}} e^- \rightarrow qqqq\nu$	23.2%	12.0%	18,540
$e^+ \gamma_{\text{EPA}} \rightarrow qqqq\nu$	18.2%	7.5%	3,652
$e^+ \gamma_{\text{BS}} \rightarrow qqqq\nu$	23.4%	12.2%	18,770

Table 2.10.: Selection summary at 1.4TeV. The subscript EPA or BS for the incoming photons indicate whether the photon is generated from the equivalent photon approximation or beamstrahlung. Channels omitted from this table have less than 1,500 events in the post MVA selection.

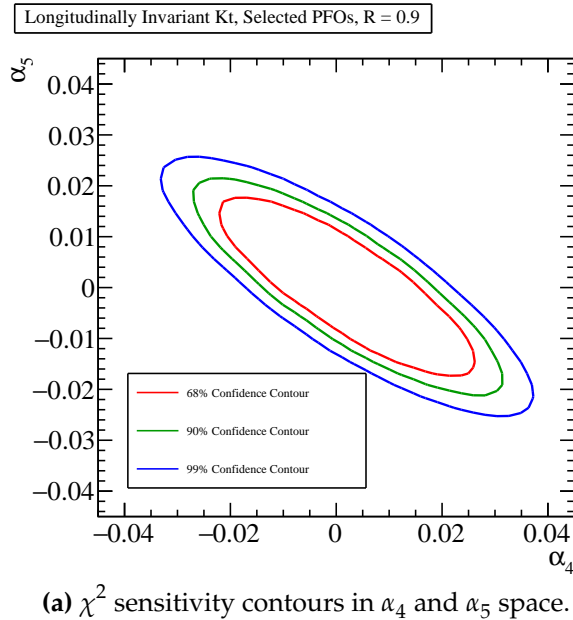
2.7.3. Pre Selection - 3 TeV

2.7.4. MVA - 3 TeV

2.8. Results

2.8.1. 1.4 TeV

The sensitivity of the CLIC experiment to the anomalous gauge couplings α_4 and α_5 at 1.4 TeV is shown in figure 2.13a. This result shows the sensitivity after the application of preselection and MVA described in sections 2.7.1 and 2.7.2 purposed to remove the included background channels, described in section 2.2. These contours yield the one σ confidence limit on the measurement of α_4 to the range -0.00831, 0.0130 and similarly for the measurement of α_5 the range is -0.00606, 0.00904.



(a) χ^2 sensitivity contours in α_4 and α_5 space.

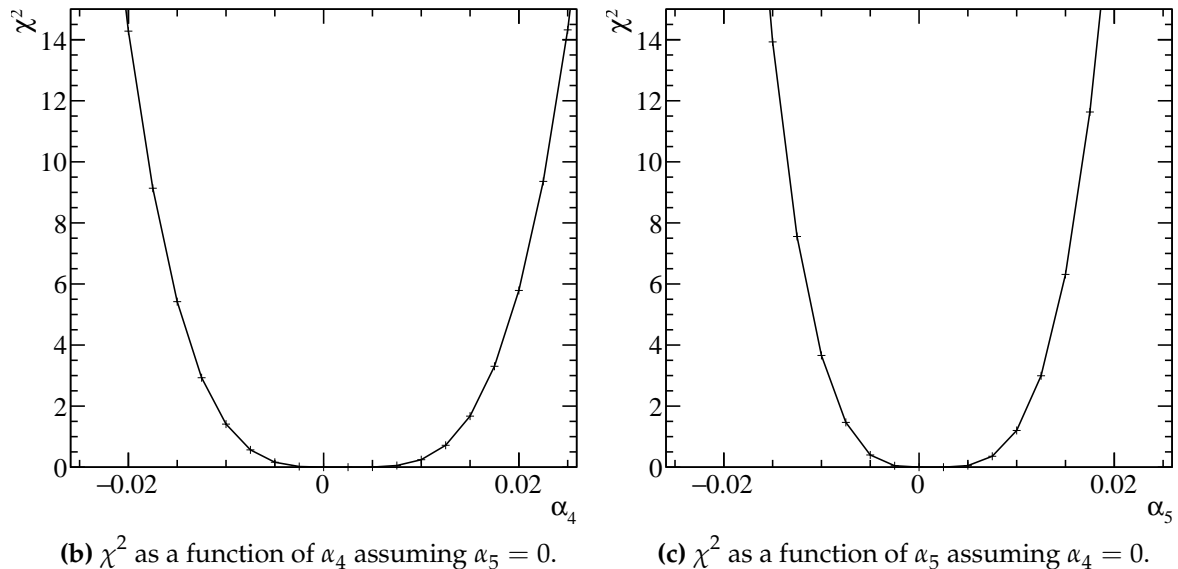


Figure 2.13.: χ^2 sensitivity distributions at 1.4 TeV arising from a fit to $\cos\theta_{\text{jets}}^*$. Results include the effect of backgrounds after the application of preselection and MVA.

Final State	Raw Event Numbers	$p_T > 100 \text{ GeV}$	$p_T > 100 \text{ GeV} \&$ $M_{\text{Vis}} > 200 \text{ GeV}$	$p_T > 100 \text{ GeV} \&$ $M_{\text{Vis}} > 200 \text{ GeV} \&$ $N_{\text{Isolated Leptons}} = 0$
$e^+ e^- \rightarrow \nu\nu qqqq$	143,000	106,600	99,390	99,130
$e^+ e^- \rightarrow l\nu qqqq$	213,200	129,800	127,300	82,880
$e^+ e^- \rightarrow llqqqq$	338,600	32,750	31,010	23,550
$e^+ e^- \rightarrow qqqq$	1,093,000	40,180	37,360	37,300
$e^+ e^- \rightarrow \nu\nu qq$	2,634,000	1,333,000	380,100	379,500
$e^+ e^- \rightarrow l\nu qq$	11,120,000	4,240,000	2,479,000	1,836,000
$e^+ e^- \rightarrow llqq$	6,639,000	131,400	84,980	54,780
$e^+ e^- \rightarrow qq$	5,897,000	79,440	66,790	66,730
$\gamma_{\text{EPA}} e^- \rightarrow qqqqe^-$	575,600	57,920	54,640	34,480
$\gamma_{\text{BS}} e^- \rightarrow qqqqe^-$	2,004,000	99,930	90,750	83,440
$e^+ \gamma_{\text{EPA}} \rightarrow qqqqe^+$	575,600	57,990	54,290	34,190
$e^+ \gamma_{\text{BS}} \rightarrow qqqqe^+$	2,002,000	100,300	90,830	83,960
$\gamma_{\text{EPA}} e^- \rightarrow qqqq\nu$	108,400	63,780	60,660	46,380
$\gamma_{\text{BS}} e^- \rightarrow qqqq\nu$	414,700	233,800	215,600	213,600
$e^+ \gamma_{\text{EPA}} \rightarrow qqqq\nu$	108,400	64,230	61,130	46,720
$e^+ \gamma_{\text{BS}} \rightarrow qqqq\nu$	414,400	236,400	219,000	217,000
$\gamma_{\text{EPA}} \gamma_{\text{EPA}} \rightarrow qqqq$	805,400	54,010	48,720	37,730
$\gamma_{\text{EPA}} \gamma_{\text{BS}} \rightarrow qqqq$	3,828,000	150,800	131,600	114,500
$\gamma_{\text{BS}} \gamma_{\text{EPA}} \rightarrow qqqq$	3,825,000	150,600	133,600	116,900
$\gamma_{\text{BS}} \gamma_{\text{BS}} \rightarrow qqqq$	18,010,000	123,500	115,400	105,000

Table 2.11.: Number of events passing the various cuts applied in the preselection at 3 TeV. Event numbers are normalised to the correct luminosity for CLIC at 3 TeV. p_T is the transverse momentum of the event, M_{Vis} is the visible mass and $N_{\text{Isolated Leptons}}$ is the number of isolated leptons in the event. In the above table $q \in u, \bar{u}, d, \bar{d}, s, \bar{s}, c, \bar{c}, b$ or \bar{b} while $l \in e^\pm, \mu^\pm$ or τ^\pm and $\nu \in \nu_e, \nu_\mu$ and ν_τ . The subscript EPA or BS for the incoming photons indicate whether the photon is generated from the equivalent photon approximation or beamstrahlung.

Final State	Raw Event Numbers	Post MVA Selection Numbers
$e^+e^- \rightarrow \nu\nu qqqq$	143,000	64,750
$e^+e^- \rightarrow l\nu qqqq$	213,200	23,310
$e^+e^- \rightarrow llqqqq$	338,600	2,409
$e^+e^- \rightarrow qqqq$	1,093,000	3,069
$e^+e^- \rightarrow \nu\nu qq$	2,634,000	19,040
$e^+e^- \rightarrow l\nu qq$	11,120,000	27,910
$e^+e^- \rightarrow llqq$	6,639,000	786
$e^+e^- \rightarrow qq$	5,897,000	1,335
$\gamma_{\text{EPA}} e^- \rightarrow qqqqe^-$	575,600	2,860
$\gamma_{\text{BS}} e^- \rightarrow qqqqe^-$	2,004,000	8,352
$e^+ \gamma_{\text{EPA}} \rightarrow qqqqe^+$	575,600	3,063
$e^+ \gamma_{\text{BS}} \rightarrow qqqqe^+$	2,002,000	8,090
$\gamma_{\text{EPA}} e^- \rightarrow qqqq\nu$	108,400	17,950
$\gamma_{\text{BS}} e^- \rightarrow qqqq\nu$	414,700	108,000
$e^+ \gamma_{\text{EPA}} \rightarrow qqqq\nu$	108,400	17,980
$e^+ \gamma_{\text{BS}} \rightarrow qqqq\nu$	414,400	109,700
$\gamma_{\text{EPA}} \gamma_{\text{EPA}} \rightarrow qqqq$	805,400	3,058
$\gamma_{\text{EPA}} \gamma_{\text{BS}} \rightarrow qqqq$	3,828,000	9,812
$\gamma_{\text{BS}} \gamma_{\text{EPA}} \rightarrow qqqq$	3,825,000	8,880
$\gamma_{\text{BS}} \gamma_{\text{BS}} \rightarrow qqqq$	18,010,000	2,213

Table 2.12.: Number of events passing the MVA selection at 3 TeV. Event numbers are normalised to the correct luminosity for CLIC at 3 TeV. The subscript EPA or BS for the incoming photons indicate whether the photon is generated from the equivalent photon approximation or beamstrahlung.

Final State	ϵ_{presel}	ϵ_{BDT}	N_{BDT}
$e^+e^- \rightarrow \nu\nu qqqq$	69.4%	45.3%	64,750
$e^+e^- \rightarrow l\nu qqqq$	38.9%	10.9%	23,310
$e^+e^- \rightarrow \nu\nu qq$	14.4%	0.7%	19,040
$e^+e^- \rightarrow l\nu qq$	16.5%	0.3%	27,910
$\gamma_{\text{BS}} e^- \rightarrow qqqqe^-$	4.1%	0.4%	8,352
$e^+ \gamma_{\text{BS}} \rightarrow qqqqe^+$	4.2%	0.4%	8,090
$\gamma_{\text{EPA}} e^- \rightarrow qqqq\nu$	42.8%	16.6%	17,950
$\gamma_{\text{BS}} e^- \rightarrow qqqq\nu$	51.6%	26.0%	108,000
$e^+ \gamma_{\text{EPA}} \rightarrow qqqq\nu$	43.1%	16.6%	17,980
$e^+ \gamma_{\text{BS}} \rightarrow qqqq\nu$	52.3%	26.5%	109,700
$\gamma_{\text{EPA}} \gamma_{\text{BS}} \rightarrow qqqq$	3.0%	0.3%	9,812
$\gamma_{\text{BS}} \gamma_{\text{EPA}} \rightarrow qqqq$	3.1%	0.2%	8,880

Table 2.13.: Selection summary at 3 TeV. The subscript EPA or BS for the incoming photons indicate whether the photon is generated from the equivalent photon approximation or beamstrahlung. Channels omitted from this table have less than 6,000 events in the post MVA selection.

Appendix A.

Pointless extras

*“Le savant n’étudie pas la nature parce que cela est utile;
il l’étudie parce qu’il y prend plaisir,
et il y prend plaisir parce qu’elle est belle.”*

— Henri Poincaré, 1854–1912

Appendices (or should that be “appendices”?) make you look really clever, ‘cos it’s like you had more clever stuff to say than could be fitted into the main bit of your thesis. Yeah. So everyone should have at least three of them...

A.1. Anomalous Gauge Coupling Quartic Vertices Of Relevance in Vector Boson Scattering

The anomalous gauge couplings involving α_4 and α_5 arise in EFT through the addition of the following terms to the Lagrangian.

$$\text{Tr}(V^\mu V_\nu) \text{Tr}(V^\nu V_\mu) \text{ and } [\text{Tr}(V^\mu V_\mu)]^2 \quad (\text{A.1})$$

Where V_μ is defined in the following way.

$$V_\mu = \Sigma (D_\mu \Sigma)^\dagger \quad (\text{A.2})$$

and Σ , the Higgs field matrix, is defined as.

$$\Sigma = \exp\left(-\frac{i}{v} \mathbf{w}\right) \quad (\text{A.3})$$

Where $\mathbf{w} = w^a \sigma^a$. w^a are the ... and σ^a are the Pauli spin matrices. The covariant derivative of the Higgs field matrix is

$$D_\mu \Sigma = \left(\partial_\mu + \frac{ig}{2} W_\mu - \frac{ig'}{2} B_\mu \sigma^3 \right) \Sigma \quad (\text{A.4})$$

For clarity consider the unitarity gauge where $\mathbf{w} = 0$, which implies $\Sigma = 1$. In this gauge V_μ takes the following form.

$$\begin{aligned} V_\mu &= \frac{i}{2} (g W_\mu^i \sigma^i - g' B_\mu \sigma^3) = \frac{i}{2} \begin{pmatrix} g W_\mu^3 - g' B_\mu & g(W_\mu^1 - iW_\mu^2) \\ g(W_\mu^1 + iW_\mu^2) & -g W_\mu^3 + g' B_\mu \end{pmatrix} \\ &= \frac{i}{2} \begin{pmatrix} \sqrt{g^2 + g'^2} Z_\mu & g\sqrt{2} W_\mu^+ \\ g\sqrt{2} W_\mu^- & \sqrt{g^2 + g'^2} Z_\mu \end{pmatrix} \end{aligned}$$

Where the relationship between the mass and gauge symmetry basis are as follows.

$$W_\mu^+ = \frac{1}{\sqrt{2}} (W_\mu^1 - iW_\mu^2) \quad (\text{A.5})$$

$$W_\mu^- = \frac{1}{\sqrt{2}} (W_\mu^1 + iW_\mu^2) \quad (\text{A.6})$$

$$Z_\mu = c_w W_\mu^3 - s_w B_\mu \quad (\text{A.7})$$

$$A_\mu = s_w W_\mu^3 + c_w B_\mu \quad (\text{A.8})$$

With $c_w = \frac{g}{\sqrt{g^2 + g'^2}}$ and $s_w = \frac{g'}{\sqrt{g^2 + g'^2}}$. Consider the expansion of the terms to be included in the Lagrangian.

$$V^\mu V_\nu = \frac{-1}{4} \begin{pmatrix} \sqrt{g^2 + g'^2} Z^\mu & g\sqrt{2}W^{+\mu} \\ g\sqrt{2}W^{-\mu} & \sqrt{g^2 + g'^2} Z^\mu \end{pmatrix} \begin{pmatrix} \sqrt{g^2 + g'^2} Z_\nu & g\sqrt{2}W_\nu^+ \\ g\sqrt{2}W_\nu^- & \sqrt{g^2 + g'^2} Z_\nu \end{pmatrix} \quad (\text{A.9})$$

$$\text{Tr}[V^\mu V_\nu] = \frac{-1}{2}((g^2 + g'^2)Z^\mu Z_\nu + g^2 W^{+\mu} W_\nu^- + g^2 W^{-\mu} W_\nu^+) \quad (\text{A.10})$$

$$\text{Tr}[V^\mu V_\nu] \text{Tr}[V_\mu V^\nu] = \frac{(g^2 + g'^2)^2}{4}(Z^\mu Z_\mu)^2 + g^2(g^2 + g'^2)(Z^\mu Z^\nu W_\mu^- W_\nu^+) \quad (\text{A.11})$$

$$+ \frac{g^4}{2}(W^{-\mu} W_\mu^+)^2 + \frac{g^4}{2}(W^{-\mu} W^{+\nu} W_\mu^- W_\nu^+) \quad (\text{A.12})$$

$$\text{Tr}[V^\mu V_\mu]^2 = \frac{(g^2 + g'^2)^2}{4}(Z^\mu Z_\mu)^2 + g^2(g^2 + g'^2)(Z^\mu Z^\nu W_\mu^- W_\nu^+) \quad (\text{A.13})$$

$$+ g^4(W^{-\mu} W_\mu^+)^2 \quad (\text{A.14})$$

These two terms change the cross section for the vector boson scattering processes at CLIC that involve $ZZ \rightarrow ZZ$, $W^+W^- \rightarrow ZZ$, $ZZ \rightarrow W^+W^-$ and $W^+W^- \rightarrow W^+W^-$.

$$\text{Z} \quad \text{Z} \quad \text{Z} \quad \text{Z} \subset (\alpha_4 + \alpha_5) \frac{(g^2 + g'^2)^2}{4} \quad (\text{A.15})$$

$$Z \quad \begin{matrix} W \\ \diagdown \\ \diagup \\ W \end{matrix} \quad Z \subset (\alpha_4 + \alpha_5)g^2(g^2 + g'^2) \quad (\text{A.16})$$

$$W \quad \begin{matrix} W \\ \diagdown \\ \diagup \\ W \end{matrix} \quad W \subset (\alpha_4 + 2\alpha_5)\frac{g^4}{2} \text{ and } \frac{g^4}{2}\alpha_4 \quad (\text{A.17})$$

A.2. χ^2 Contour Plots for Jet Algorithm Optimisation

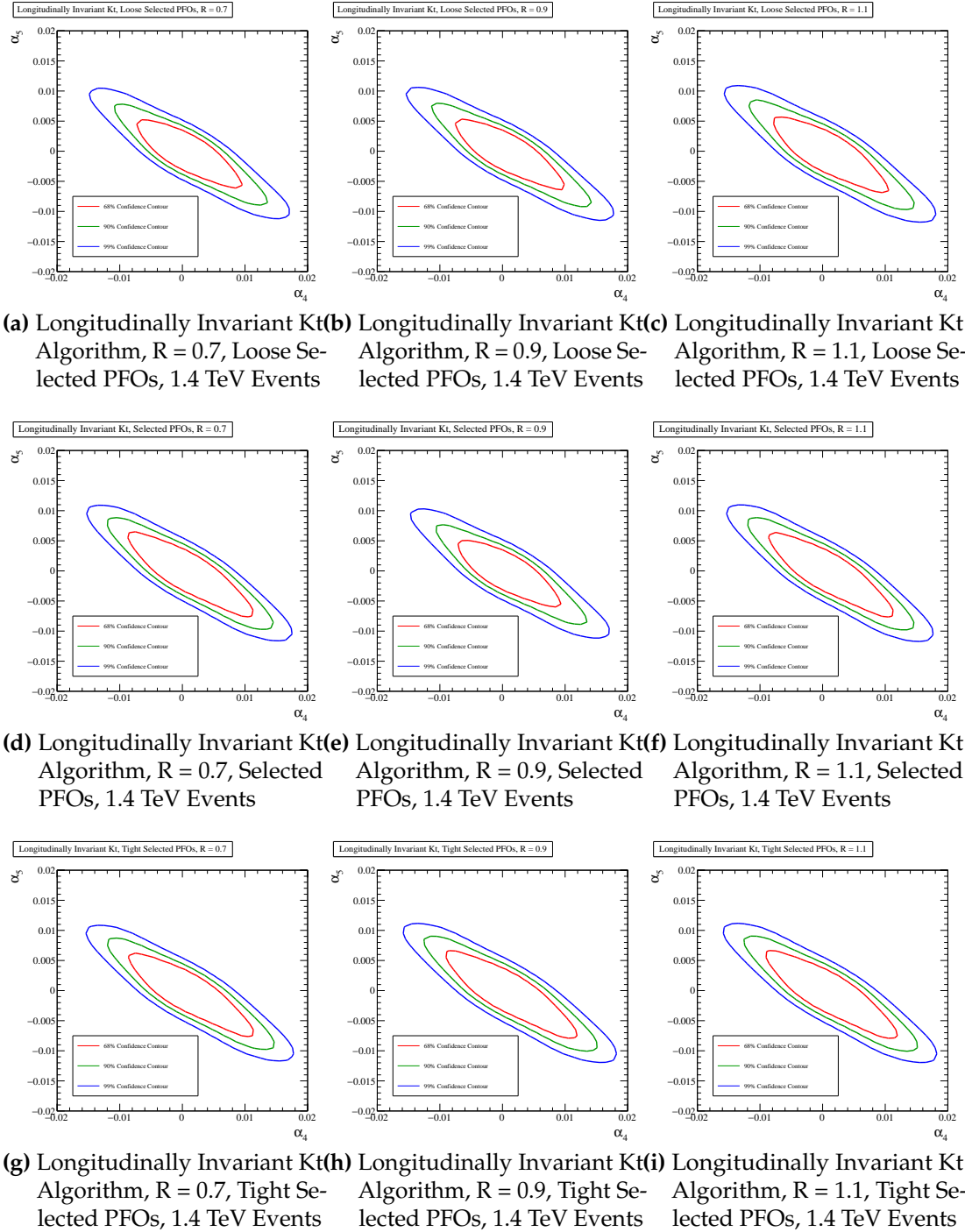


Figure A.1: χ^2 Sensitivity contours for the $qqqq\nu\nu$ final state arising from a fit to $\cos\theta_{\text{jets}}^*$ at 1.4 TeV for different values of jet reconstruction parameters.

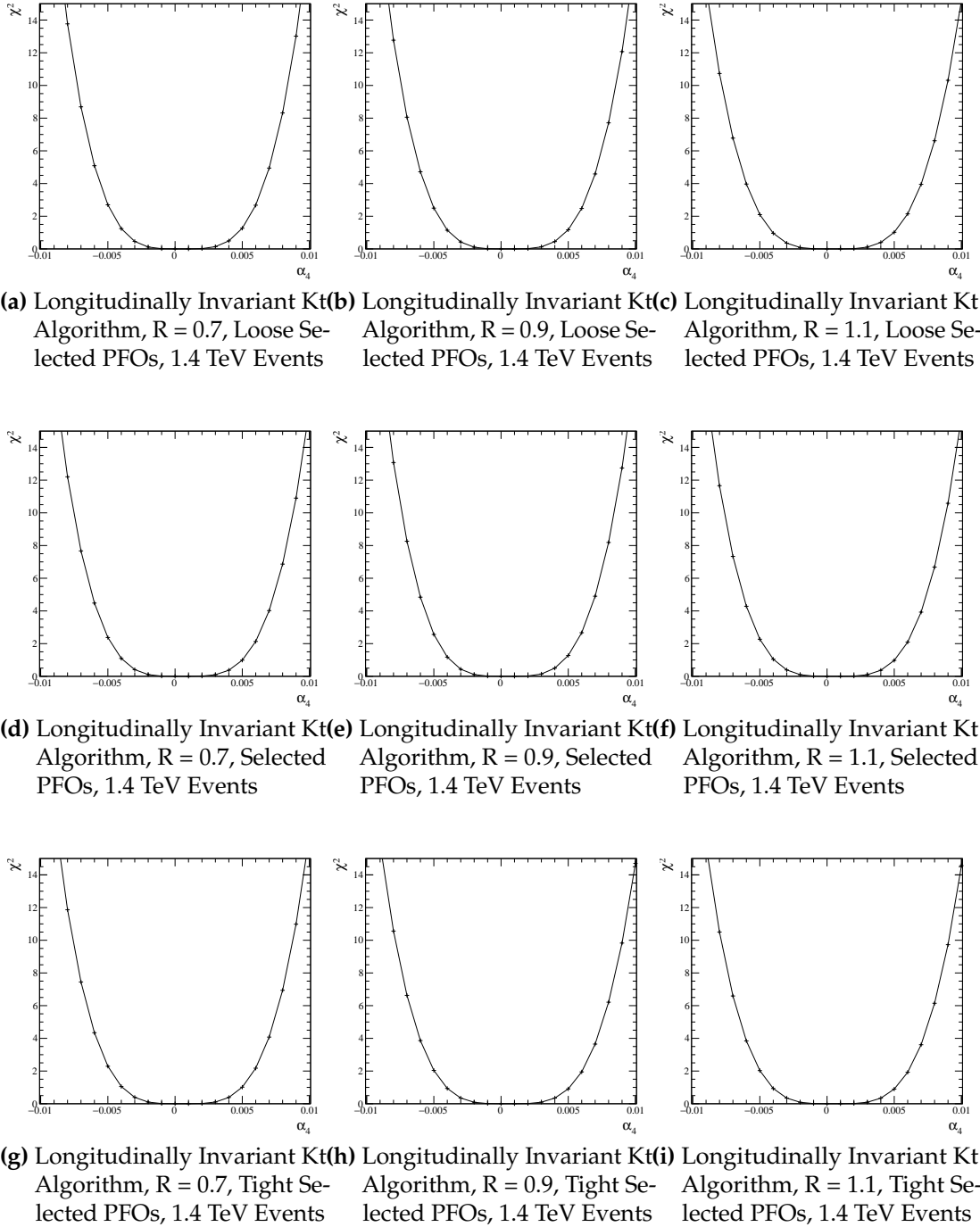


Figure A.2: χ^2 as a function of α_4 assuming $\alpha_5 = 0$ for the $qqqq\nu\nu$ final state arising from a fit to $\cos\theta_{\text{jets}}^*$ at 1.4 TeV for different values of jet reconstruction parameters.

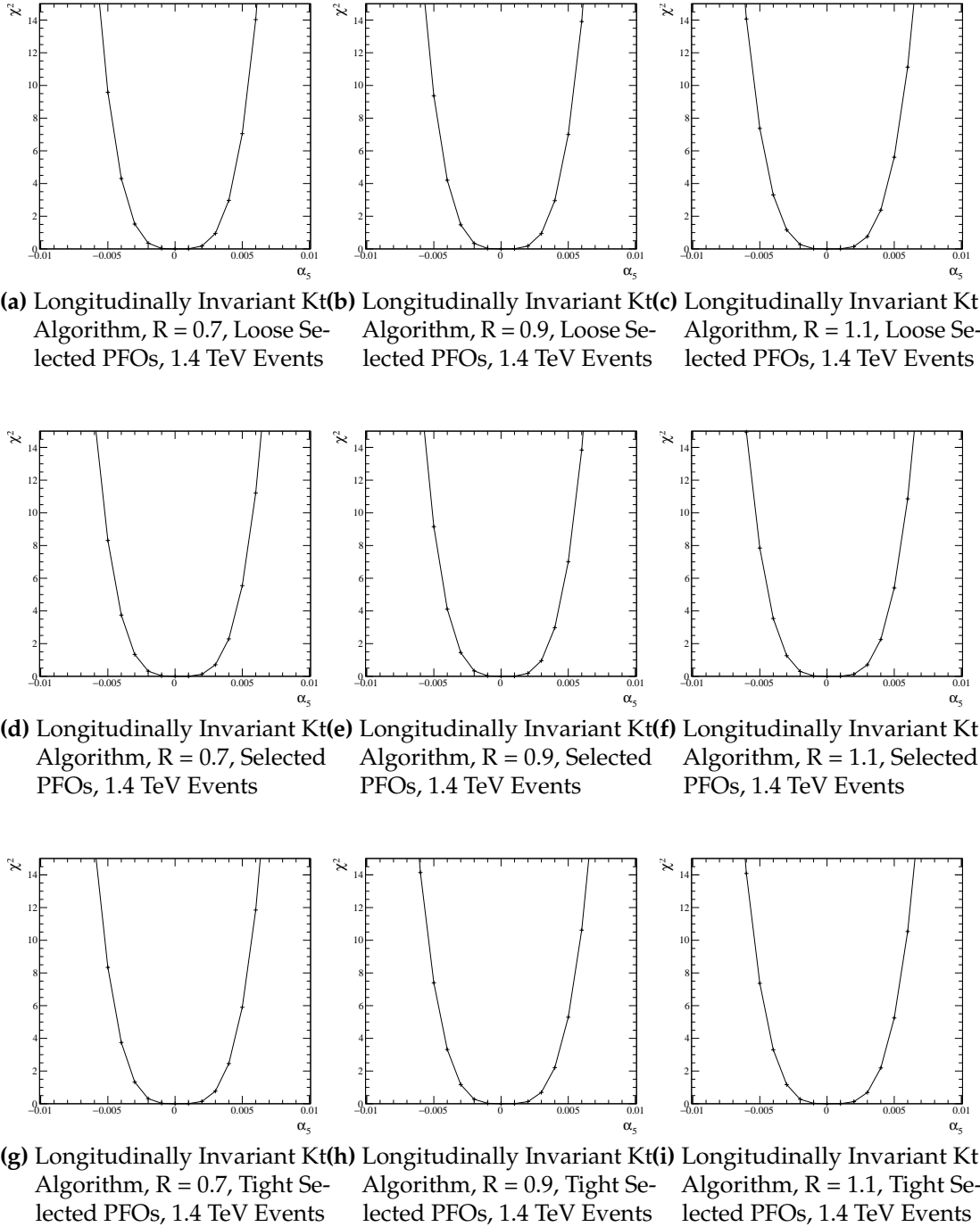
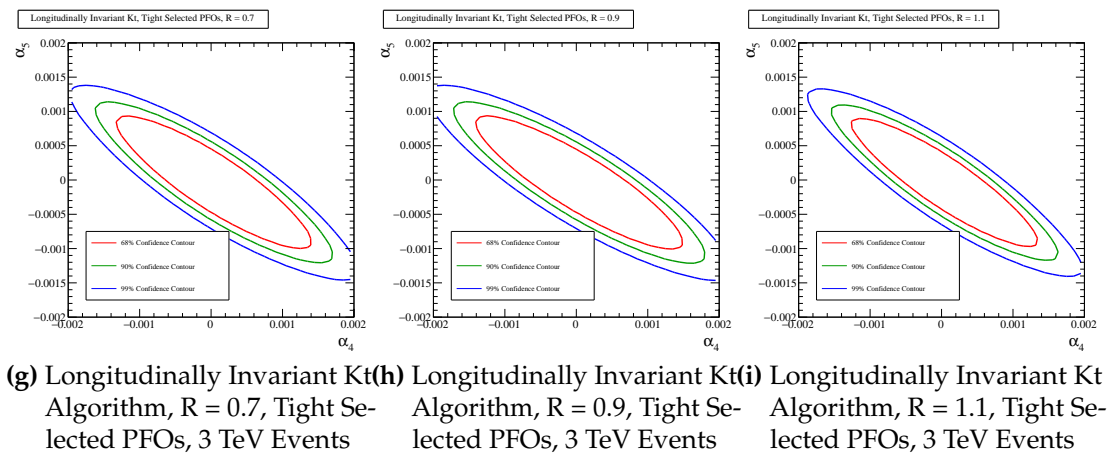
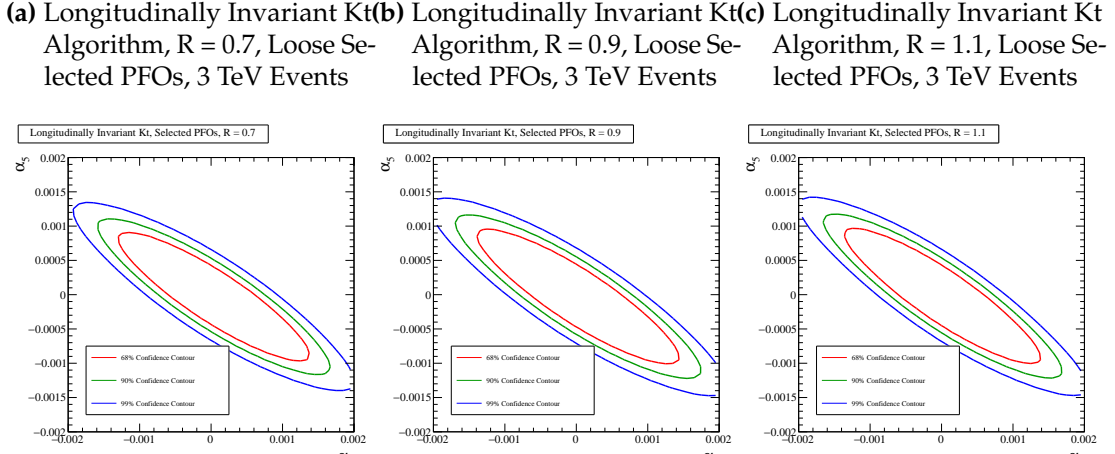
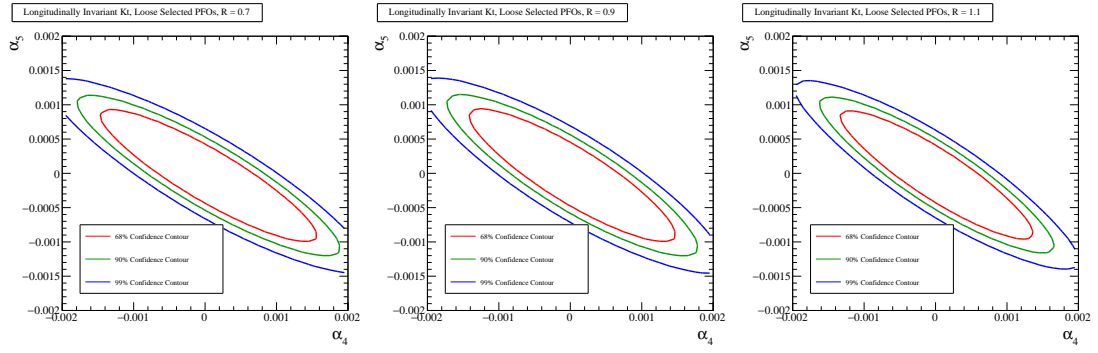


Figure A.3: χ^2 as a function of α_5 assuming $\alpha_4 = 0$ for the $qqqq\nu\nu$ final state arising from a fit to $\cos\theta_{\text{jets}}^*$ at 1.4 TeV for different values of jet reconstruction parameters.



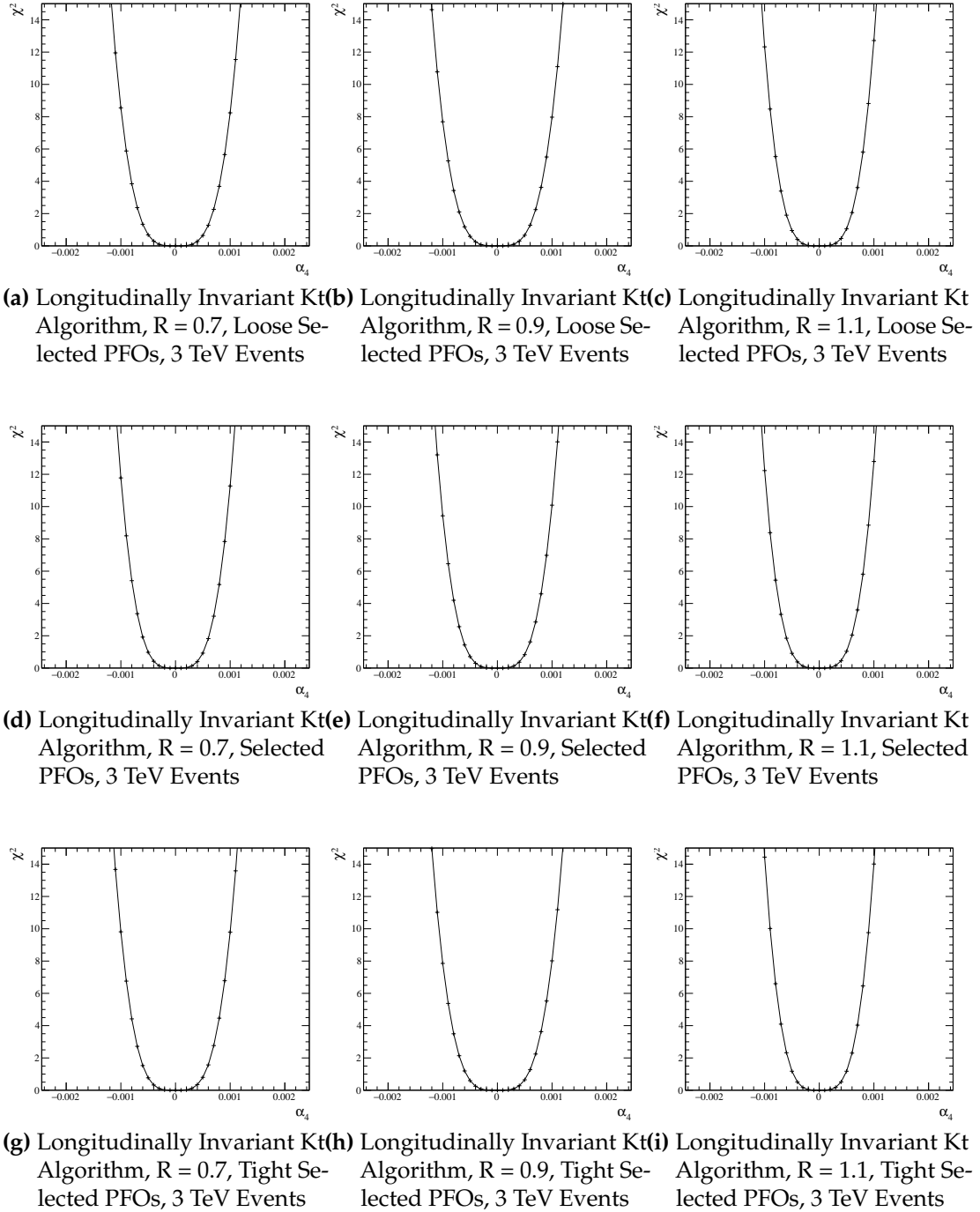


Figure A.4: χ^2 as a function of α_4 assuming $\alpha_5 = 0$ for the $qqqq\nu\nu$ final state arising from a fit to $\cos\theta_{\text{jets}}^*$ at 3 TeV for different values of jet reconstruction parameters.

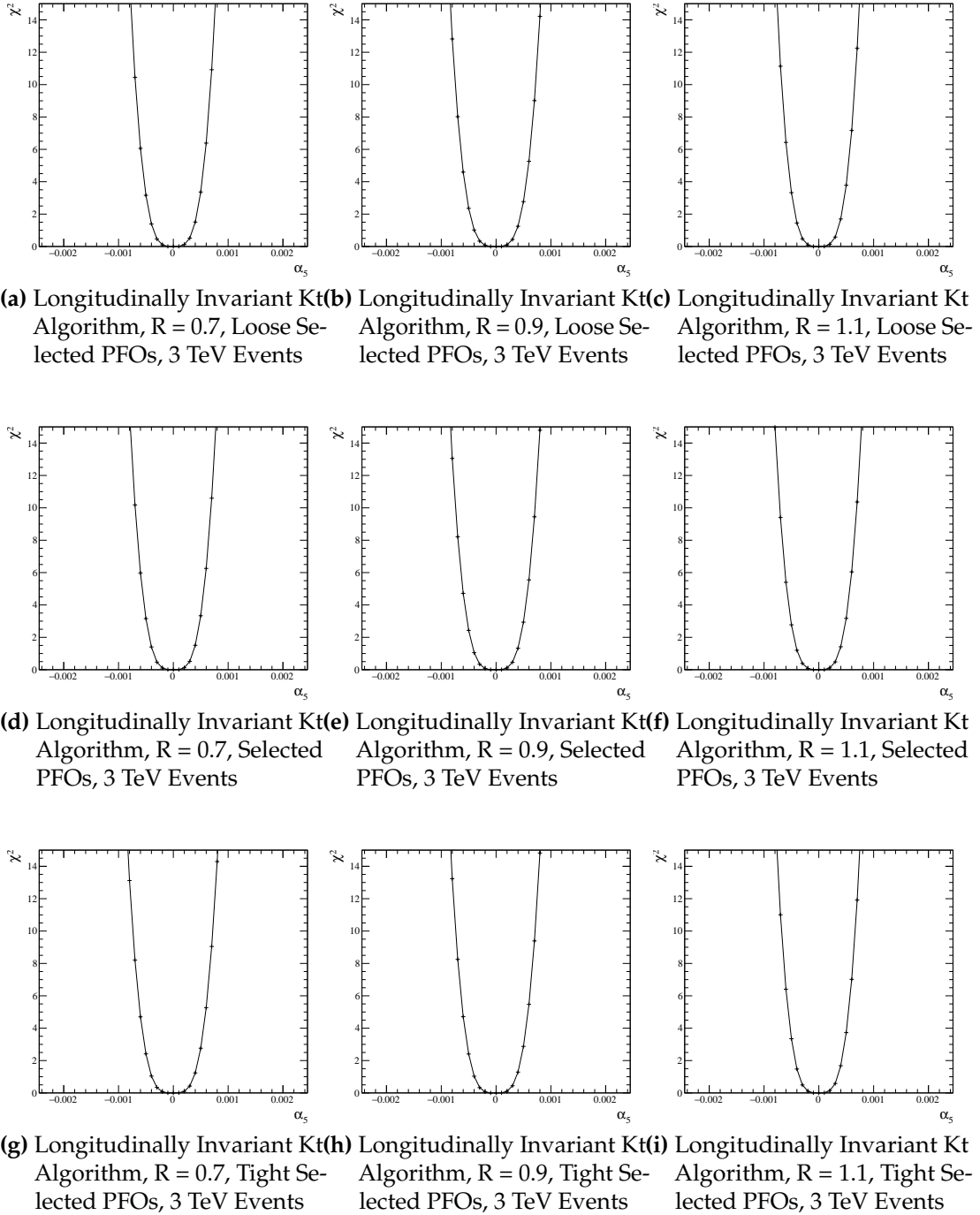


Figure A.5: χ^2 as a function of α_5 assuming $\alpha_4 = 0$ for the $qqqq\nu\nu$ final state arising from a fit to $\cos\theta_{\text{jets}}^*$ at 3 TeV for different values of jet reconstruction parameters.

Colophon

This thesis was made in L^AT_EX 2 _{ϵ} using the “hepthesis” class [3].

Bibliography

- [1] Toshinori Abe et al. The International Large Detector: Letter of Intent. 2010, 1006.3396.
- [2] S. Agostinelli et al. GEANT4: A Simulation toolkit. *Nucl. Instrum. Meth.*, A506:250–303, 2003.
- [3] Andy Buckley. The heptesis L^AT_EX class.
- [4] Matteo Cacciari, Gavin P. Salam, and Gregory Soyez. FastJet User Manual. *Eur. Phys. J.*, C72:1896, 2012, 1111.6097.
- [5] F. Gaede. Marlin and LCCD: Software tools for the ILC. *Nucl. Instrum. Meth.*, A559:177–180, 2006.
- [6] Andreas Hoecker, Peter Speckmayer, Joerg Stelzer, Jan Therhaag, Eckhard von Toerne, and Helge Voss. TMVA: Toolkit for Multivariate Data Analysis. *PoS*, ACAT:040, 2007, physics/0703039.
- [7] Wolfgang Kilian, Thorsten Ohl, and Jurgen Reuter. WHIZARD: Simulating Multi-Particle Processes at LHC and ILC. *Eur. Phys. J.*, C71:1742, 2011, 0708.4233.
- [8] Lucie Linssen, Akiya Miyamoto, Marcel Stanitzki, and Harry Weerts. Physics and Detectors at CLIC: CLIC Conceptual Design Report. 2012, 1202.5940.
- [9] J. S. Marshall, A. M^Ãajnnich, and M. A. Thomson. Performance of Particle Flow Calorimetry at CLIC. *Nucl. Instrum. Meth.*, A700:153–162, 2013, 1209.4039.
- [10] P. Mora de Freitas and H. Videau. Detector simulation with MOKKA / GEANT4: Present and future. In *Linear colliders. Proceedings, International Workshop on physics and experiments with future electron-positron linear colliders, LCWS 2002, Seogwipo, Jeju Island, Korea, August 26-30, 2002*, pages 623–627, 2002.
- [11] Mauro Moretti, Thorsten Ohl, and Jurgen Reuter. O'Mega: An Optimizing matrix

- element generator. 2001, hep-ph/0102195.
- [12] C. Patrignani et al. Review of Particle Physics. *Chin. Phys.*, C40(10):100001, 2016.
- [13] B. Pilicer, Helmut Burkhardt, Laurent Gatignon, Andrea Latina, Ercan Pilicer, Daniel Schulte, İlhan Tapan, and Rogelio Tomás. Study of Muon Backgrounds in the CLIC Beam Delivery System. In *Proceedings, 6th International Particle Accelerator Conference (IPAC 2015): Richmond, Virginia, USA, May 3-8, 2015*, page TUPTY032, 2015.
- [14] András Sailer. *Radiation and Background Levels in a CLIC Detector due to Beam-Beam Effects*. PhD thesis, CERN, 2012-05-09.
- [15] Taikan Suehara and Tomohiko Tanabe. LCFIPlus: A Framework for Jet Analysis in Linear Collider Studies. *Nucl. Instrum. Meth.*, A808:109–116, 2016, 1506.08371.
- [16] M. A. Thomson. Particle Flow Calorimetry and the PandoraPFA Algorithm. *Nucl. Instrum. Meth.*, A611:25–40, 2009, 0907.3577.

List of figures

1.1. Energy resolution as a function of photon energy for the nominal ILD detector for both the silicon and scintillator options.	2
1.2. Jet energy resolution as a function of ECal cell size.	4
1.3. Jet energy resolution breakdown as a function of ECal transverse granularity for 45 and 250 GeV jets. Results are given for both the silicon and scintillator ECal options.	5
1.4. Energy resolution as a function of ECal transverse granularity for 100 GeV photons. Results are given for both the silicon and scintillator ECal options.	5
1.5. Jet energy resolution as a function of longitudinal granularity in the ECal.	7
1.6. Jet energy resolution breakdown as a function of ECal longitudinal granularity for 45 and 250 GeV jets. Results are given for both the silicon and scintillator ECal options.	8
1.7. Energy resolution as a function of ECal longitudinal granularity for 100 GeV photons. Results are given for both the silicon and scintillator ECal options.	8
1.8. Jet energy resolution as a function of HCal cell size.	11
1.9. Jet energy resolution breakdown as a function of HCal transverse granularity for 45 and 250 GeV jets.	12
1.10. Energy resolution as a function of HCal transverse granularity for 50 GeV K_L^0	12
1.11. Jet energy resolution as a function of longitudinal granularity in the HCal.	13

1.12. Jet energy resolution breakdown as a function of HCal longitudinal granularity for 45 and 250 GeV jets.	14
1.13. Energy resolution as a function of HCal longitudinal granularity for 50 GeV K_L^0	15
1.14. Jet energy resolution as a function of the number of nuclear interaction lengths in the HCal.	16
1.15. Jet energy resolution breakdown as a function of nuclear interaction lengths in the HCal for 45 and 250 GeV jets.	17
2.1. Event weights from Whizard for 1.4TeV $\nu\nu\text{qqqq}$ final state events.	23
2.2. Comparison of various distributions between samples used in this analysis and the official CLIC samples for the $\nu\nu\text{qqqq}$ final state at 1.4 and 3 TeV.	25
2.4. Reconstructed invariant masses for different choices of jet algorithm for 1.4 TeV and 3 TeV $\nu\nu\text{qqqq}$ events.	30
2.5. Sensitivity of $\cos\theta_{\text{jets}}^8$ to the anomalous gauge couplings α_4 and α_5 at 1.4 and 3 TeV.	34
2.6. Sensitivity of $\cos\theta_{\text{Bosons}}^8$ to the anomalous gauge couplings α_4 and α_5 at 1.4 and 3 TeV.	35
2.7. Event weights from Whizard for 1.4TeV $\nu\nu\text{qqqq}$ final state events with interpolated surface.	36
2.8. χ^2 sensitivity distributions for the $\text{qqqq}\nu\nu$ final state arising from a fit to $\cos\theta_{\text{jets}}^*$ at 1.4 TeV for the optimal jet reconstruction parameters.	39
2.9. χ^2 sensitivity distributions for the $\text{qqqq}\nu\nu$ final state arising from a fit to $\cos\theta_{\text{jets}}^*$ at 3 TeV for the optimal jet reconstruction parameters.	41
2.10. Distribution of variables cut on in the preselection at 1.4 TeV.	44
2.11. Impact of preselection and MVA on the reconstructed invariant mass of the bosons arising from jet pairing at 1.4 TeV.	47
2.12. Distribution of variables cut on in the preselection at 3 TeV.	49

2.13. χ^2 sensitivity distributions at 1.4 TeV arising from a fit to $\cos\theta_{\text{Jets}}^*$. Results include the effect of backgrounds after the application of preselection and MVA.	51
A.1. χ^2 Sensitivity contours for the $qqqq\nu\nu$ final state arising from a fit to $\cos\theta_{\text{Jets}}^*$ at 1.4 TeV for different values of jet reconstruction parameters.	59
A.2. χ^2 as a function of α_4 assuming $\alpha_5 = 0$ for the $qqqq\nu\nu$ final state arising from a fit to $\cos\theta_{\text{Jets}}^*$ at 1.4 TeV for different values of jet reconstruction parameters.	60
A.3. χ^2 as a function of α_5 assuming $\alpha_4 = 0$ for the $qqqq\nu\nu$ final state arising from a fit to $\cos\theta_{\text{Jets}}^*$ at 1.4 TeV for different values of jet reconstruction parameters.	61
A.4. χ^2 as a function of α_4 assuming $\alpha_5 = 0$ for the $qqqq\nu\nu$ final state arising from a fit to $\cos\theta_{\text{Jets}}^*$ at 3 TeV for different values of jet reconstruction parameters.	63
A.5. χ^2 as a function of α_5 assuming $\alpha_4 = 0$ for the $qqqq\nu\nu$ final state arising from a fit to $\cos\theta_{\text{Jets}}^*$ at 3 TeV for different values of jet reconstruction parameters.	64

List of tables

1.1.	Nominal ILD detector model ECal configuration.	3
1.2.	Transverse granularity layout of various ECal models considered in this study.	7
1.3.	Nominal ILD detector model HCal configuration.	10
1.4.	Transverse granularity layout of various HCal models considered. . . .	14
1.5.	Depth and layout of various HCal models considered.	16
2.1.	Cross section for selected processes for given value of α_4 and α_5 at 1.4 TeV.	22
2.2.	Cross section for selected processes for given value of α_4 and α_5 at 3 TeV.	22
2.3.	1σ precision on measurement of α_4 for different jet reconstruction parameters considering pure signal at 1.4 TeV.	40
2.4.	1σ precision on measurement of α_5 for different jet reconstruction parameters considering pure signal at 1.4 TeV.	40
2.5.	1σ precision on measurement of α_4 for different jet reconstruction parameters considering pure signal at 3 TeV.	40
2.6.	1σ precision on measurement of α_5 for different jet reconstruction parameters considering pure signal at 3 TeV.	42
2.8.	Number of events passing the various cuts applied in the preselection at 1.4TeV.	45
2.9.	Number of events passing the MVA selection at 1.4TeV.	48
2.10.	Selection summary at 1.4TeV.	50

2.11. Number of events passing the various cuts applied in the preselection at 3 TeV.	52
2.12. Number of events passing the MVA selection at 3 TeV.	53
2.13. Selection summary at 3 TeV.	54